

Rochester Institute of Technology

RIT Digital Institutional Repository

Theses

2-2014

Compensation of Extreme Ultraviolet Lithography Image Field Edge Effects Through Optical Proximity Correction

Chris Maloney

Follow this and additional works at: <https://repository.rit.edu/theses>

Recommended Citation

Maloney, Chris, "Compensation of Extreme Ultraviolet Lithography Image Field Edge Effects Through Optical Proximity Correction" (2014). Thesis. Rochester Institute of Technology. Accessed from

This Thesis is brought to you for free and open access by the RIT Libraries. For more information, please contact repository@rit.edu.

**COMPENSATION OF EXTREME ULTRAVIOLET
LITHOGRAPHY IMAGE FIELD EDGE EFFECTS
THROUGH OPTICAL PROXIMITY CORRECTION**

by
CHRIS MALONEY

A thesis submitted in partial fulfillment of the requirements
For the degree of Master of Science in
Microelectronic Engineering

Kate Gleason College of Engineering
Department of Electrical and Microelectronic Engineering
Rochester Institute of Technology
Rochester, NY

February 2014

Author: _____
Chris Maloney

Approved by: _____
Robert Pearson, Ph.D.

Approved by: _____
Bruce W. Smith, Ph.D.

Approved by: _____
Dale Ewbank, Ph.D.

Approved by: _____
Sohail Dianat, Ph.D.

ABSTRACT

Kate Gleason College of Engineering
Rochester Institute of Technology

Degree: Master of Science **Program:** Microelectronic Engineering

Name of Candidate: Chris Maloney

Title: Compensation of extreme ultraviolet lithography image field edge effects through optical proximity correction

For EUVL to be enabled for HVM, the printing of densely spaced die must be allowed. To achieve this requirement, a mitigation strategy to compensate for field edge effects is vital. This study has two goals. First, we will show that field edge effects can be modeled for reticles with an absorber border and for those with an etched ML border. The second is to investigate the limitations that exist when compensating for field edge effects with OPC, including image quality, REMA blade stability and OoB variability. This thesis shows that for different reticles different mitigation strategies are required in order to enable EUV HVM.

ACKNOWLEDGMENTS

There are many people that I owe my gratitude too, but first I have to give glory to God. He has been with me my entire life watching over me, even if I wasn't aware of it. I am so blessed to have been given the opportunities to succeed and the support of family and friends throughout the entire way.

Of course I have to thank my patient wife Kelly. You supported me the entire way, no matter what situation we were in. You even moved to Belgium, just to be with me to chase after my ambitions. You are the most selfless person I know, I love you.

I am grateful to my parents, John and Diane Maloney. Dad, you have always shown me the importance of hard work to be successful in anything. And Mom, somehow you succeeded (I like to think) in raising me to be a polite and respectful young man, thank you for never giving up on me.

To my advisor Dr. Bruce Smith, thank you for giving me the opportunity to pursue a graduate degree and providing me with such a life changing internship. This has opened doors to participate in cutting edge research, network with those making industry decisions and also make new friends.

I am also so grateful for those that I have worked with at Mentor Graphics and IMEC such as John Sturtevant, James Word, Geert Vandenberghe, Eric Hendrickx and Vincent Wiaux for all of your guidance along the way. Also thank you to my group members at RIT, Peng Xie, Germain Fenger, Burak Balyav, Monica Sears and Andrew

Estroff, for all of your discussions to better understand all of the aspects of lithography.
Lastly I would like to thank SRC and Mentor Graphics for the support in funding my
education.

Table of Contents

1.	Background	1
1.1	Historical Overview	1
1.2	Lithography	1
1.2.1	Image Formation	2
1.2.2	Resolution	7
1.2.3	Modulation	9
1.2.4	Depth of Focus	10
1.2.5	Flare	12
1.2.6	OPC	16
1.3	EUV Lithography	16
1.3.1	System Overview	17
1.3.2	Shadowing	18
1.3.3	REMA Blades	22
1.3.4	Field Edge Effect	23
1.3.5	OoB Radiation	25
1.3.6	Stochastic effects	26
2.	Research Motivation	29
2.1	Problem	29
2.2	Objectives	30
3.	Approach	31
3.1	Experimental	31

3.1.1	ML etched mask.....	31
3.1.2	Dense CH Array Measurements	32
3.1.3	Measuring OoB variability	33
3.2	Simulations.....	35
3.2.1	Field edge effect model fitting.....	35
3.2.2	OPC.....	36
3.2.3	Image Quality.....	37
3.2.4	REMA Blade Positioning after OPC	38
3.2.5	Simulating OoB variability.....	39
4.	Results.....	41
4.1	CH measurements	41
4.2	Modeling	43
4.2.1	70nm thick absorbers	43
4.2.2	Etched ML border.....	44
4.2.3	Extrapolating to 51nm and 84nm absorbers	45
4.2.4	OPC.....	49
4.3	Requirements for design correction	50
4.3.1	Good image quality.....	51
4.3.1.1	Aerial image	51
4.3.1.2	Process window	53
4.3.1.3	Stochastic effect on LCDU.....	58
4.3.2	Stable REMA blade position	60
4.3.3	Stable OoB contribution	64

5. Alternative Mitigation Strategy	67
6. Conclusions.....	69
7. References.....	74

LIST OF FIGURES

Figure 1. Schematic of Köhler illumination for optical lithography.	2
Figure 2. Binary mask function with pitch p	3
Figure 3. Fourier transform of the mask function in frequency space.	5
Figure 4. Visualizing the objective lens as a linear filter.	6
Figure 5. Impact of objective lens NA on imaging.	7
Figure 6. DOF calculated as the width of the red ellipse after evaluating the process window of multiple features.	12
Figure 7. Mask function exhibiting flare.	13
Figure 8. PSF and TIS function used to describe the impact of flare on imaging.	15
Figure 9. a) Resist contour without OPC. b) Resist contour after OPC implementing SRAFs and serifs.	16
Figure 10. Schematic of ASML NXE:3100.	18
Figure 11. Schematic representation of how a EUV scanner creates shadow.	19
Figure 12. Effective angle of incidence for horizontal and vertical lines.	20
Figure 13. Simplified geometric sketch of absorber shadowing, depicting the full range of incident angles and their contribution to shadowing.	21
Figure 14. Shadowing resulting in asymmetries between ± 1 reflected diffraction orders.	21
Figure 15. Illustration of image border reflections overlapping with neighboring die.	22
Figure 16. Illustration of REMA blade placement and resulting penumbra.	23

Figure 17.a) Ideal die stitching. b) Actual die stitching showing overlapping image borders overexposing the image field.	25
Figure 18. Theoretical reflectivity for Mo/Si ML mirrors.	26
Figure 19. a.) Continuum approximation used in resist modeling. b.) Stochastic resist modeling showing photon and resist reactant randomness.	27
Figure 20. Four contact hole cross sections generated using Prolith Stochastic Resist Modeling (red=resist).	28
Figure 21. Cross-section of etched ML border.	32
Figure 22. Reticle layout showing measurement positions of 36nm dense contact holes in black.	33
Figure 23. DUV reflectivity in multilayer, absorber and aluminum blanks.	34
Figure 24. EUV reflectivity in aluminum.	34
Figure 25. Dose to clear using both aluminum blank and multilayer blank.	35
Figure 26. Flaremap generation for field edge effects.	36
Figure 27. Example of how OPC will be used to correct 36nm dense contact holes.	37
Figure 28. Illustration of how the REMA blade may vary from its nominal position.	39
Figure 29. 36nm dense contact holes measured at distances extending diagonally from the corner of the image field.	42
Figure 30. 36nm dense contact holes measured at distances extending diagonally from the corner of the image field using a reticle with an etched ML border.	43
Figure 31. a.)Field edge effects from 70nm Hoya absorber at corner of the field modeled to fit measurement data. b.) Calibrated flaremap showing measurement points in black.	44

Figure 32. a.)Field edge effects from etched ML border at corner of the field modeled to fit measurement data. b.) Calibrated flaremap showing measurement points in black. ...	45
Figure 33. EUV absorber reflectivity for three different absorber types.....	46
Figure 34. a.)Model extrapolated to three different absorber types. b.) Simulated CD comparison between features in the center of the field features at the corner of the field.	48
Figure 35. CD bias after applying OPC as a function of flare (field edge effects are lumped into flare).....	49
Figure 36. CD bias after applying OPC for a 70nm absorber border and an etched ML border.	50
Figure 37. Aerial image comparison between 36nm dense CHs at the center of the field vs. features at the corner of the field for three different absorbers a.) 51nm Hoya b.) 70nm Hoya c.) 84nm AGC.	52
Figure 38. NILS corresponding to the simulated aerial image for 36nm dense CHs at the center of the field and features at the corner of the field after OPC corresponding to three different absorbers.	53
Figure 39. Simulated 36nm dense CH process window for features in the corner of the field seeing the effects of three overlapping fields after OPC a.) 51nm Hoya absorber b.) 70nm Hoya absorber c.) 84nm AGC absorber.....	55
Figure 40. Simulated 36nm dense CH exposure latitude vs. depth of focus curves for features in the corner of the field seeing the effects of three overlapping fields after OPC a.) 51nm Hoya absorber b.) 70nm Hoya absorber c.) 84nm AGC absorber.....	57

Figure 41. Simulated LCDU for 36nm dense CHs in the center of the field and in the corner of the field after OPC.....	59
Figure 42. Simulated CD for 36nm dense CHs for different REMA blade positions before OPC a.)70nm Hoya absorber border b.) Etched ML border.....	62
Figure 43. Simulated CD variation for different borders when shifting the REMA blade after correcting with OPC at the nominal REMA blade position.	63
Figure 44. Measurement of OoB component for IMEC’s NXE:3100.....	65
Figure 45. Simulated CD variation for etched ML border when OoB radiation varies after correcting with OPC at the center of the OoB radiation range.	66
Figure 46. Thicker absorber border potential mitigation strategy.	68

LIST OF TABLES

Table 1. EUV and DUV reflectivity at 6° for four different border types.....	46
Table 2. Simulated 36nm dense CH process window results after correcting with OPC for field edge effects.	58
Table 3. Simulated 36nm dense CH process window results after correcting with OPC for field edge effects.	59
Table 4. Flaremaps generated for multiple REMA blade positions.....	61

1. Background

1.1 Historical Overview

We live in a world where we are always surrounded by technology, whether it is computers, smart phones, tablets etc. As the demand for newer, faster and smaller devices increases, the semiconductor industry continues to be the driving force behind these new technologies. This industry was born in 1947 with the invention of the first transistor at Bell labs [1]. Just ten years later the integrated circuit was invented [2]. Instead of having large packaged discrete electronics, these devices could now be made smaller and all placed together on a single substrate. At the same time, lithography techniques were being developed to print these integrated circuits [3],[4].

Lithography is a process that involves the use of a template to print circuit patterns onto actual devices. This process has been driving the semiconductor industry since it was introduced [5],[6],[7]. In order to fabricate smaller, faster and more efficient devices, the need for smaller line widths and higher density of features becomes essential. In 1971, the first microprocessor held 2,300 $10\mu\text{m}$ transistors within 12mm^2 [8]; modern microprocessors hold as many as 5 billion 22nm transistors within 363mm^2 [9]. The shrink of device size and increase of packing density has been enabled by lithography.

1.2 Lithography

1.2.1 Image Formation

A typical projection lithography system is depicted in Figure 1. This basic system implements Köhler illumination, which is the same method that optical microscopes operate. In this type of system, the source is focused onto the pupil plane with the purpose of imaging the mask pattern at the wafer plane. When the diffraction pattern from the mask reaches the projection optics, it will be in the Fraunhofer region of diffraction and the image formation at the wafer can be described using Fourier analysis and synthesis [10], [11], [12].

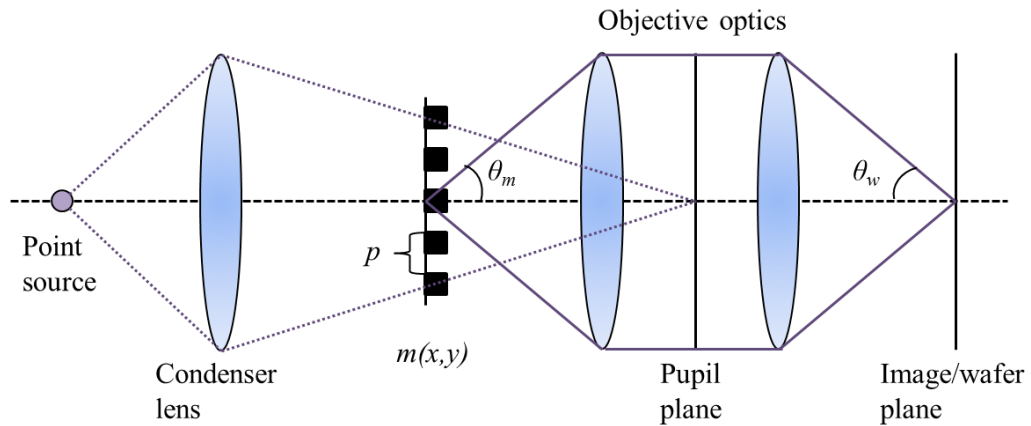


Figure 1. Schematic of Köhler illumination for optical lithography.

When discussing these systems it is the most simple to think of the mask as a binary grating of infinite lines and spaces at a certain pitch (p) being illuminated by a coherent point source at normal incidence. A mask like this can also be thought of as a square wave or a rect function with width equal to half the pitch convolved with an infinite sum of periodic delta functions. This mask can be described mathematically as a function, $m(x)$.

$$m(x) = \text{rect}\left(\frac{x}{p/2}\right) \otimes \sum_{n=-\infty}^{\infty} \delta(x - np) \quad (1)$$

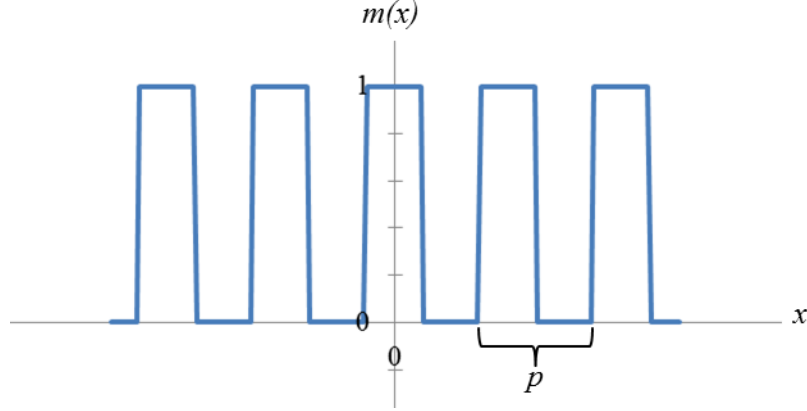


Figure 2. Binary mask function with pitch p .

When light is diffracted by the mask, the integer number of diffraction orders (m) follow the grating formula as:

$$\sin\theta_m = \pm \frac{m\lambda}{p}. \quad (2)$$

What is hidden by this equation is the fact that all orders are not of equal magnitude. The diffracted light can be represented in frequency space as the Fourier transform of the mask function in frequency space.

$$M(u) = \mathcal{F}\{m(x)\} = \frac{1}{2} \text{sinc}\left(\frac{u}{2u_0}\right) \sum_{n=-\infty}^{\infty} \delta(u - nu_0) \quad (3)$$

Where the frequency of the mask grating is represented as,

$$u_0 = \frac{1}{p}. \quad (4)$$

The comb function will produce impulse functions corresponding to each diffraction order as defined by the diffraction equation whose amplitude is a function of the encapsulating sinc function. Looking at the plot of this result (Figure 3), one can also determine what diffraction orders will be captured by the objective lens. To determine this one must first have an understanding of the definition of numerical aperture (NA).

The NA of a system can be better understood as

$$NA_o = n \sin \theta_w , \quad (5)$$

where, n is the index of refraction of image recording media, in modern 193nm projection systems the media used is water with an index of 1.44. The value of θ_w can be defined as the collection angle of the objective optics. The maximum value of NA_o that has been achieved for optical lithography in a production environment is 1.35. The NA_o can be included on the plot of the Fourier transform of the mask function to show which orders will be captured by the objective lens. To do this one must treat the objective lens as a linear filter ($H(u)$) and it should be multiplied by the diffraction orders ($M(u)$) to act as filter. Figure 4 shows how NA_o can be plotted and only the diffracted orders within the limits drawn are collected by the objective lens.

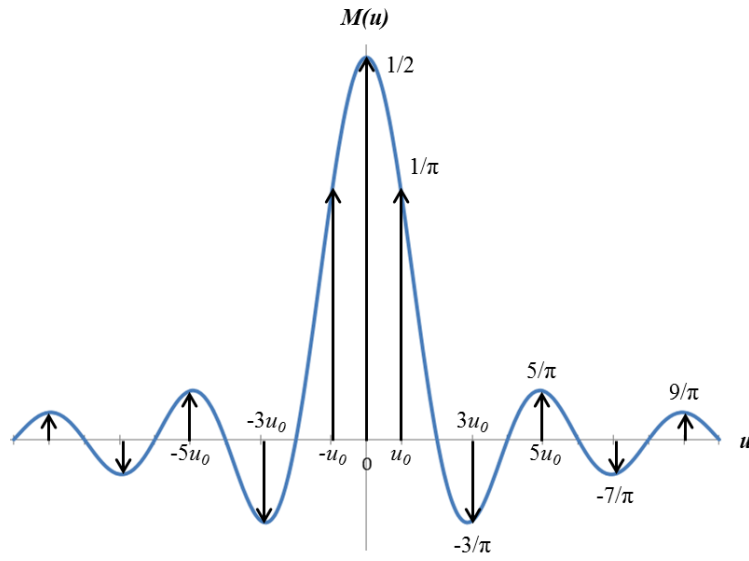


Figure 3. Fourier transform of the mask function in frequency space.

$$H(u) = \begin{cases} 1 & \text{if } |u| < \frac{NA}{\lambda} \\ 0 & \text{if } |u| > \frac{NA}{\lambda} \end{cases} \quad (6)$$

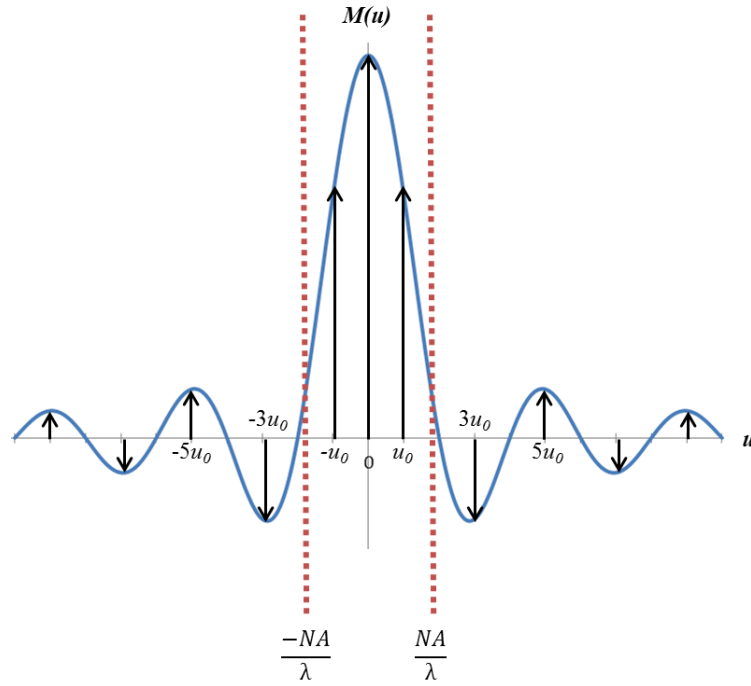


Figure 4. Visualizing the objective lens as a linear filter.

Once this information is obtained, it is then possible to evaluate the electric field (E) and therefor the irradiance of the aerial image ($I=|E^2|$). Using Fourier series expansion and utilizing only the information captured by the objective lens one can construct the resulting electric field as:

$$E(x) = \frac{1}{2} + \frac{2}{\pi} \cos(2\pi u_0 x) - \frac{2}{3\pi} \cos(2\pi(3u_0)x) + \frac{2}{5\pi} \cos(2\pi(5u_0)x) \dots \quad (7)$$

Each \pm diffraction order pair collected by the object lens contributes to one of the partial sum terms in the Fourier series. To create an ideal replica image of the mask, all diffraction orders must be collected; in reality this is impossible. To image in high contrast photoresist, the high frequency information is not needed and only orders as high as ± 1 are required.

Figure 5 shows how diffraction orders are collected by the objective lens while varying NA_o , how the resulting electric fields respond and finally the irradiance of the aerial image.

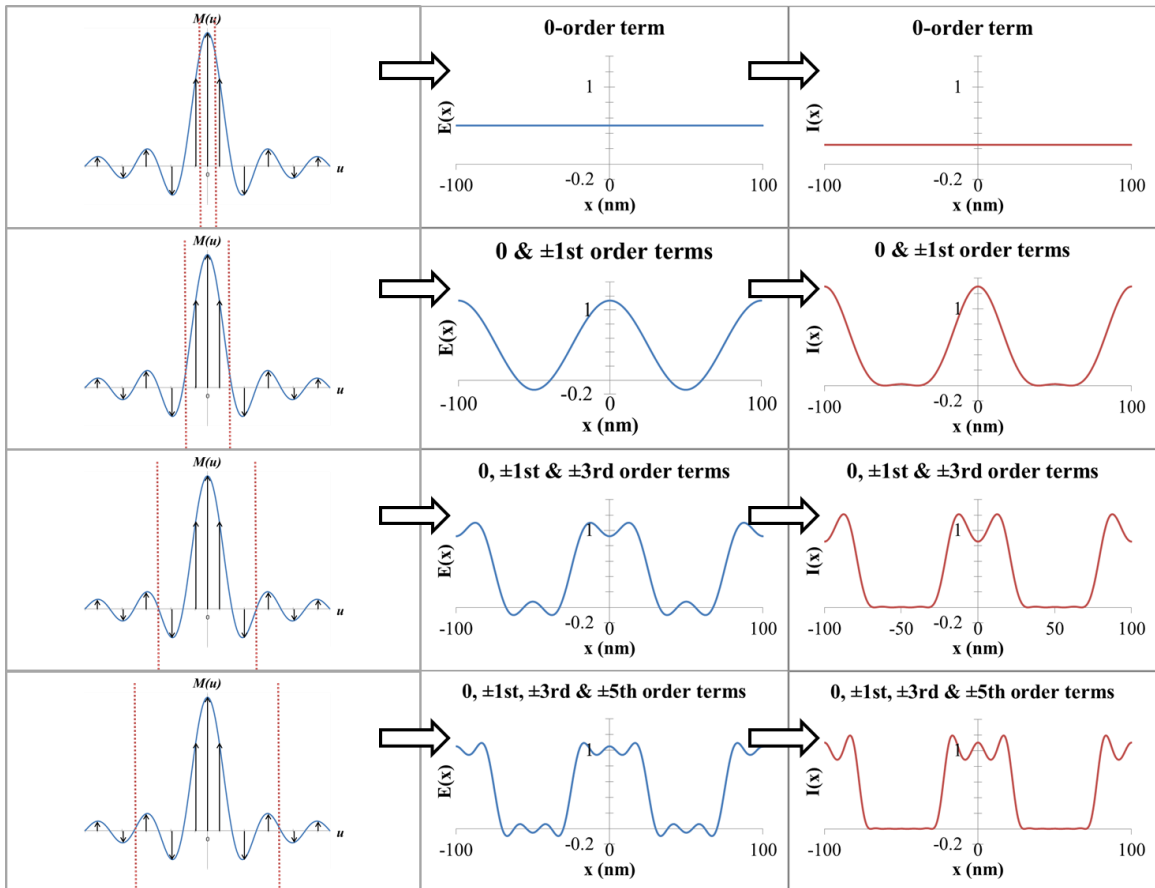


Figure 5. Impact of objective lens NA on imaging.

1.2.2 Resolution

The ultimate resolution of a diffraction limited system can be determined by the Rayleigh criterion as shown in Equation (8) [13], [14].

$$R = \frac{k_1 \lambda}{NA_o}, \quad (8)$$

In this equation, the resolution is the minimum half pitch that can be imaged, λ is the exposure wavelength, k_1 is a process dependent parameter with a lower limit of 0.25 and NA_o is the numerical aperture of the objective optics. For state-of-the-art production technology, ArF excimer lasers emit deep-ultraviolet (DUV) light at 193nm as the illumination wavelength [15]. The k_1 factor has historically been reduced by using various resolution enhancement technologies (RET) such as phase shift masking (PSM) [16], [17] off-axis illumination (OAI) [18], source polarization [19], source mask optimization (SMO) [20], and optical proximity correction (OPC) [21].

To look further into the k_1 factor, we must look at its dependence on the partial coherence of the system. Partial coherence, or σ is defined as the ratio of condenser optics NA to objective optics NA.

$$\sigma = \frac{NA_c}{NA_o} \quad (9)$$

Looking at the extremes of partially coherent imaging, a coherent system would have $\sigma=0$, while an incoherent system yields $\sigma=1$. Changing the degree of partial coherence also changes the k_1 factor as follows:

$$k_1 = \frac{0.5}{\sigma + 1}. \quad (10)$$

Now it is clear why the k_l lower limit of 0.25 exists. This can only be achieved while using completely incoherent illumination. Using this information the Raleigh criterion can now be extended to include partial coherence.

$$R = \frac{0.5\lambda}{(\sigma + 1)NA_o} \quad (11)$$

1.2.3 Modulation

Image modulation is also referred to as contrast. It provides a metric to analyze the quality of the aerial image. Image modulation is defined as the normalized ratio of maximum and minimum irradiance values.

$$M = \frac{I_{max} - I_{min}}{I_{max} + I_{min}} \quad (12)$$

This metric gives a good starting point to understand the quality of a periodic image, but for more complicated feature types it is difficult to define the maximum and minimum irradiances. In these instances which are usually more common in practice, it is better to use the normalized image logs slope (NILS) as a metric of image quality. This provides a measurement of the slope of the aerial image at the location of where the feature edge is targeted. Multiplying the image log slope (ILS) by the critical dimension (CD) normalizes the equation to provide a metric than can be used to compare just about any feature type and pitch.

$$NILS = \frac{\delta \ln I(x)}{\delta x} \times CD \quad (13)$$

Another metric that is commonly used is mask error enhancement factor (MEEF). MEEF is a metric related to NILS, and is typically used more when discussing OPC, which will be defined in Section 1.2.6. MEEF describes the change in wafer CD as a result of a changing mask CD. If an image has low NILS and therefore low image modulation, then a small change in mask CD will have a dramatic impact on the wafer CD. On the contrary, high NILS and high image modulation would provide more tolerance to mask CD errors when imaging a desired CD. Equation (14) shows how MEEF is calculated; R is the reduction ratio of the system.

$$MEEF = \frac{\Delta CD_{wafer}}{\Delta CD_{mask}/R} \quad (14)$$

1.2.4 Depth of Focus

Depth of focus (DOF) provides an additional criterion that needs to be satisfied for each feature. This metric describes the amount of defocus that is acceptable when imaging a certain feature. It is an important metric to consider when imaging multiple feature types and for features with low image modulation. The resulting DOF is dependent on a number of elements such as user defined values of acceptable CD variation and exposure latitude (EL). Typical values include $\pm 5\%$ for CD variation and $\pm 10\%$ for exposure latitude. DOF is also dependent on the resist; resists that are more capable of imaging features from a poorly modulated aerial image will increase the DOF.

To measure the DOF of a system, a focus exposure matrix (FEM) is necessary. Measurements can be made at multiple focus and exposure conditions to determine which conditions provide an acceptable environment for the image to meet the specified CD variation and exposure latitude conditions. As technology generations evolve, the trend is going to shorter wavelengths to image smaller half pitches. This makes the job for the resist more and more difficult [22] as DOF decreases linearly with short wavelengths and quadratically with NA.

$$DOF \propto \frac{\lambda}{NA^2} \quad (15)$$

An example of how depth of focus is analyzed can be seen in Figure 6 [23]. In order to find the acceptable DOF for a full chip solution, these plots for different features can be overlaid on top of one another and the DOF will be calculated from the smallest remaining window. The center of this window will provide the best exposure energy and best focus for the process.

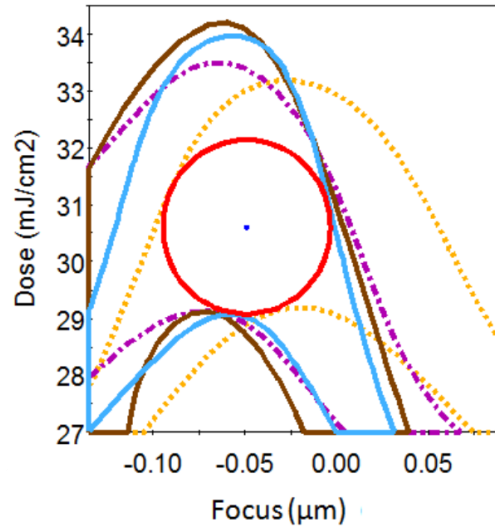


Figure 6. DOF calculated as the width of the red ellipse after evaluating the process window of multiple features.

1.2.5 Flare

Flare is defined as the total stray light in a system that reaches the image plane, and can be included in the equations used to describe the formation of an image. Flare (F) can be calculated as the ratio of dose in the ‘clear’ region over the dose in the ‘dark’ region as seen in equation (16) and depicted in Figure 7 [24].

$$m_F(x) = (1 - F) \text{rect}\left(\frac{x}{\frac{p}{2}}\right) \otimes \sum_{n=-\infty}^{\infty} \delta(x - np) + \frac{F}{2} \quad (16)$$

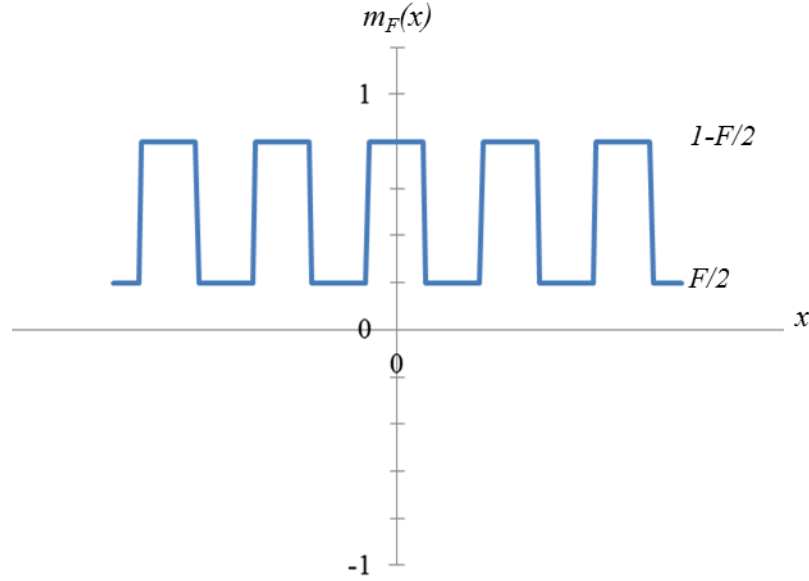


Figure 7. Mask function exhibiting flare.

The Fourier transform of a constant bias results in a delta function. If a flare value such as 0.1 is used in this equation, one can simply add together the 0 order delta functions to show that the 0 order term remains the same but the flare term in front of the sinc function reduces the amplitude of all subsequent orders.

$$M_F(u) = \mathcal{F}\{m(x)\} = \frac{1-F}{2} \text{sinc}\left(\frac{u}{2u_0}\right) \sum_{n=-\infty}^{\infty} \delta(u - nu_0) + \frac{F}{2} \delta(u) \quad (17)$$

To relate this back to the aerial image it is now possible to use Fourier series expansion to show that amplitude of the cosines that make up the aerial image decreases as a result of flare and therefore flare causes a loss of contrast.

$$I_F(x) = \left| \frac{1}{2} + (1-F) \left[\frac{2}{\pi} \cos(2\pi u_0 x) - \frac{2}{3\pi} \cos(2\pi(3u_0)x) + \frac{2}{5\pi} \cos(2\pi(5u_0)x) \dots \right] \right|^2 \quad (18)$$

This mathematical relationship is used to describe how flare effects imaging does not tell the entire story. To delve deeper into the discussion it is important to understand where flare is originated. For extreme-ultraviolet lithography (EUVL) flare is typically caused by scattering due to low, mid and high spatial-frequency range (SFR) mirror surface roughness. Flare has such a large impact on EUVL because scattering scales with wavelength as $1/\lambda^2$. Improvements have been made to state-of-the-art EUV systems to operate with flare levels around 4-5%. The total integrated scatter (TIS) of a mirror can be represented as shown in equation (19). Here, R_0 is the theoretical reflectance of the mirror, R_q is the root means squared (RMS) surface roughness of the mirror and θ_i is the angle of incidence [25].

$$TIS = R_0 \left[1 - e^{-\left(\frac{4\pi R_q \cos \theta_i}{\lambda}\right)^2} \right] \quad (19)$$

When including flare into the calculation of the image, one must first evaluate the point spread function (PSF) of the image. The PSF describes the quality of the imaging system, specifically the degree of spreading or blurring of a point source through the system. In this work, a single fractal model flare PSF will be used and is shown in equation (20).

$$PSF(r) = \begin{cases} \frac{K}{r^{n+1}}, & r > r_{min} \\ 0, & r < r_{min} \end{cases} \quad (20)$$

The modeling parameters (K , n , and r_{min}) can be optimized when compared to measurement data. K is referred to as a scaling parameter. The fractal exponent is represented by n and describes the decay of the PSF. The value r_{min} is an obscuration radius and corresponds to the radius at which the flare PSF ends and where the optical PSF begins. By knowing the TIS and PSF of the system, flare can now be included in the formation of a 2D image as shown in equation (21), where the function that describes the impact of flare on imaging is shown in Figure 8.

(21)

$$I_F(x, y) = (1 - TIS)m(x, y) + PSF(r) \otimes m(x, y)$$

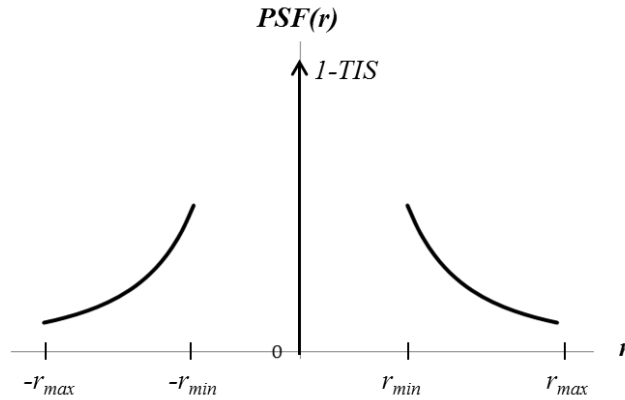


Figure 8. PSF and TIS function used to describe the impact of flare on imaging.

In EUV systems, accounting for flare is not trivial and must be included in the optical and resist models to be used for OPC. To account for flare a full-chip layout is operated on as seen in equation (21), resulting in a flare map. Using this method, OPC can be used to compensate for flare effects.

1.2.6 OPC

For state-of-the-art device generations, OPC is required to print features at their desired dimensions and also to increase their depth of focus. There are two flavors of OPC that are often implemented together. One type of OPC uses sub-resolution assist features (SRAFs) to equalize the background intensity modulation of different pitches to enhance the total depth of focus of a full chip [26]. The other type of OPC (which will be utilized in this study) is using serifs on the mask to change the shape of the main feature to help it print to the desired shape and dimension [27]. Figure 9 shows an example where both SRAFs and serifs are required.

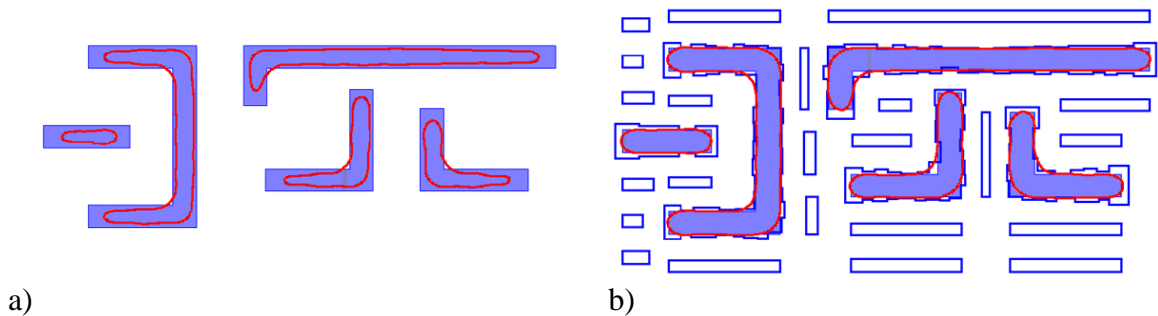


Figure 9.a)Resist contour without OPC. b)Resist contour after OPC implementing SRAFs and serifs. For this study a simplified version of this will be used since only contact holes will be discussed. For EUVL, a simple biasing of contact holes is necessary to account for both shadowing (which will be discussed in section 1.3.2) and flare effects.

1.3 EUV Lithography

1.3.1 System Overview

EUVL has been the most popular choice for next generation lithography for many years. EUVL feasibility was investigated in the 1980's, but it was not until around 2003 when EUVL took over as the most prevalent research activity for next generation lithography [28]. The actinic wavelength used in this system is 13.5 nm. For the work described in this thesis, the ASML NXE:3100 at IMEC will be used as part of the experimental procedure. This tool uses a 0.25 NA partially coherent source with a σ of 0.81 and has resolved dense lines and spaces down to 22nm half pitch. Using equation (8), it is possible to solve for the minimum k_l for this system, resulting in a value of about 0.40.

One of the major differences between EUVL and optical projection lithography is that refractive optics cannot be used for EUVL. EUV light is absorbed by nearly every material including air, requiring the system to operate in vacuum [29]. Refractive optical elements will also absorb EUV light, therefore; reflective mirrors using Bragg multilayer (ML) reflector coatings are required to manipulate the light in the system and to increase the NA. Even the mask itself must be reflective and must also be defect free.

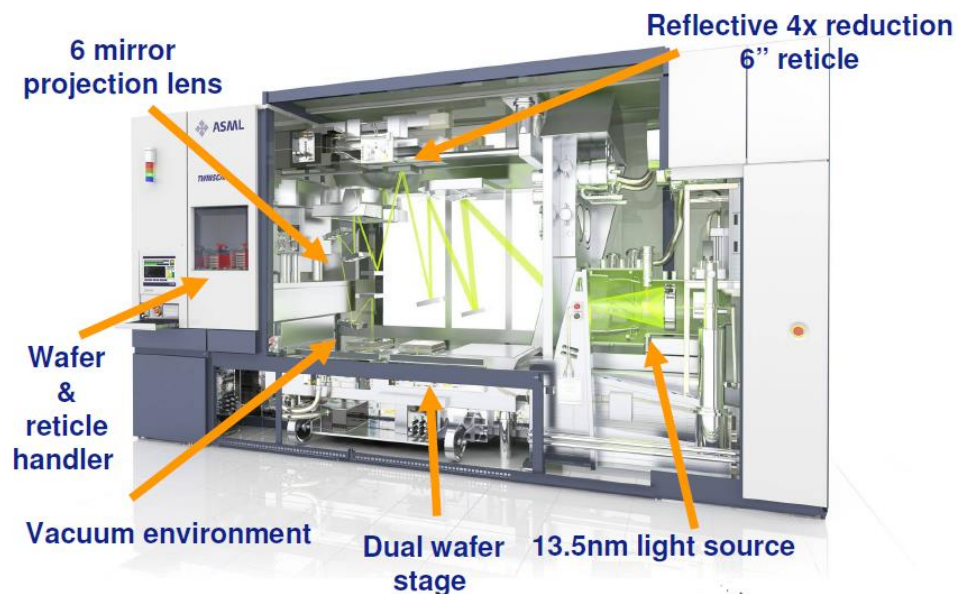


Figure 10. Schematic of ASML NXE:3100

A schematic of the NXE:3100 can be seen in Figure 10 [30], as shown there are 11 total reflection. Each mirror is limited to about 70% reflectivity resulting in a total throughput of about 2% from source to wafer. This is one of the major challenges in EUVL as it severely limits wafer throughput. This challenge directly relates to resist technology development. In order to increase wafer throughput resist must be sensitive enough to be exposed quickly but also not too quickly in order to limit shot noise [31]. Photomasks, source-power and resist are three of the main research and development areas for EUVL.

1.3.2 Shadowing

As discussed previously, EUVL requires the use of multiple mirrors. Patterns are defined on the ML mask as an additional etched absorber layer on top of the ML. The illumination is non-telecentric at the mask due to oblique illumination, but is telecentric

at the image plane. The illumination for the NXE:3100 requires a chief-ray-angle-at-object (CRAO) of 6° [32]. Through slit, the azimuthal angle (φ) will vary about $\pm 25^\circ$ but the chief ray will still maintain an incident angle (θ) of 6° for coherent illumination [33]. Therefore, the chief ray maintains the same incident angle, but it is actually rotating through slit. Each orientation of a feature will see a different ‘effective’ incident angle as described by the equation below, where ω describes the orientation of the feature as depicted in Figure 11 [33].

$$\theta_{eff}(\varphi, \omega) = \theta \cdot \cos(\varphi + \omega) \quad (22)$$

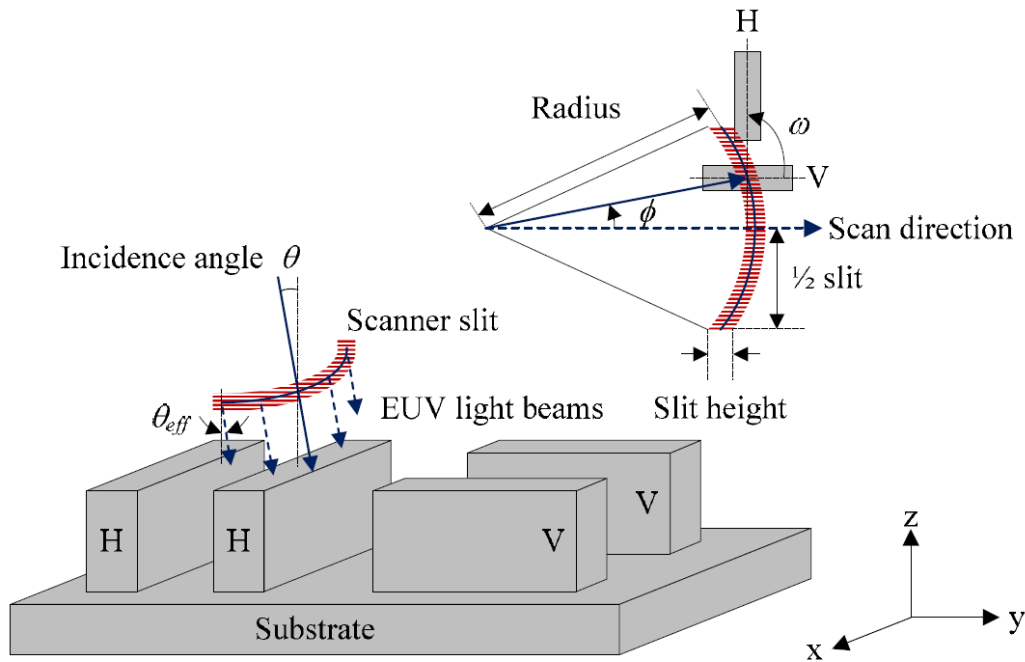


Figure 11. Schematic representation of how a EUV scanner creates shadow. The effective incident angle for horizontal and vertical line/space features have been calculated and plotted in Figure 12.

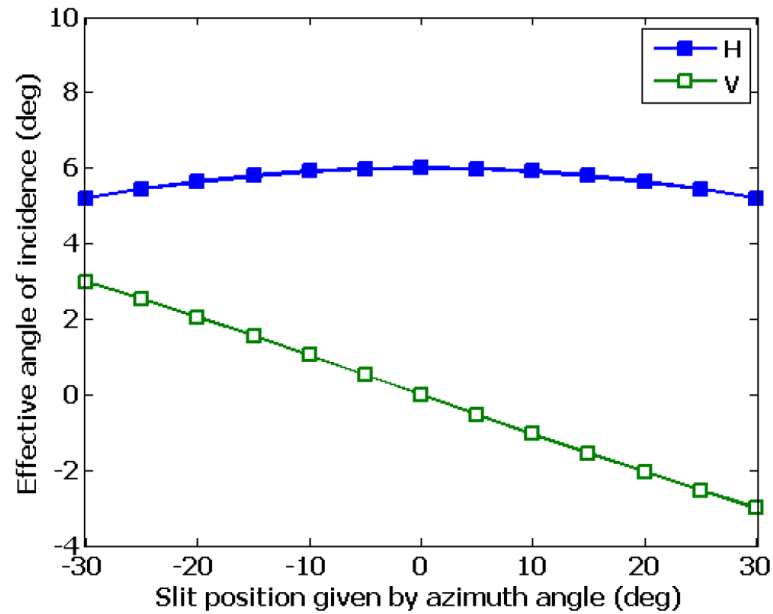


Figure 12. Effective angle of incidence for horizontal and vertical lines.

Up to this point, this discussion is only taking into account coherent illumination. If partially coherent illumination is to be used then we must expand the discussion beyond only the chief ray. In reality there is an illumination cone with a range of incident angles and in for off-axis illumination, there may be two cones (dipole) with ranges of incident angles at different chief ray incident angles. Looking at a dipole source, there will be two separate angles of incidence. One pole will produce a more acute angle of incidence and the other will result in a more oblique angle of incidence. The former will result in a weaker shadowing effect, while the latter will result in a stronger shadowing effect as depicted in Figure 13 [32].

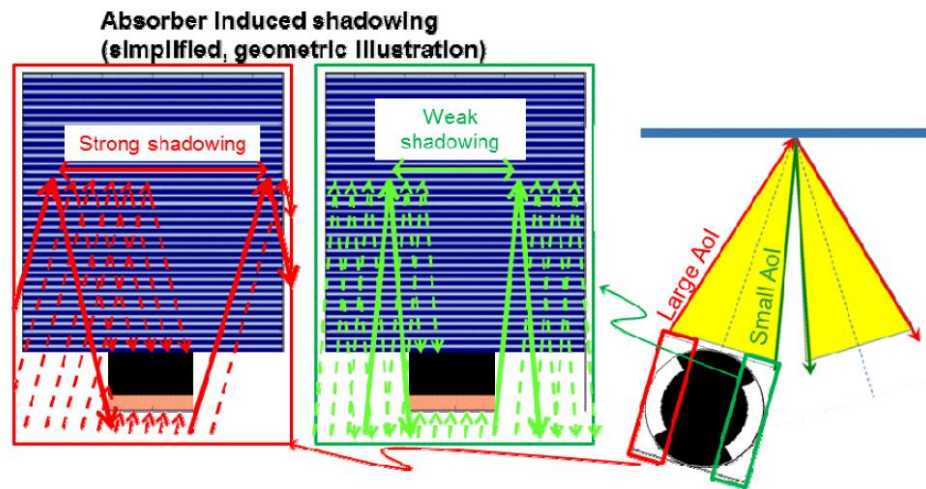


Figure 13. Simplified geometric sketch of absorber shadowing, depicting the full range of incident angles and their contribution to shadowing.

The non-telecentricity at the mask and the thickness of the absorber give rise to asymmetries in the diffracted waves. This results in differences between the +1, and -1 diffracted orders both in magnitude and in phase (Figure 14).

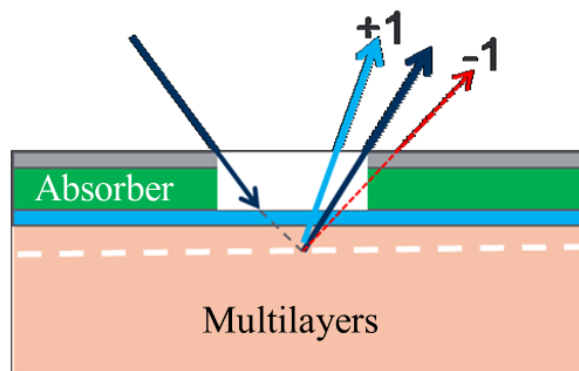


Figure 14. Shadowing resulting in asymmetries between ± 1 reflected diffraction orders. These asymmetries result in pattern fidelity degradation such as discrepancies in image CD and pattern placement [34], [35]. To suppress the shadowing effect it is desirable to use thinner absorbers.

1.3.3 REMA Blades

Reticle masking (REMA) blades are critical to the behavior at the field edge. In a production environment, REMA blades are used to block off sections of the mask that will not be exposed, and therefore surround the die that will be printed. To ensure none of the image field is blocked by the REMA blades, a portion of the ‘dark’ image border is exposed and its reflection will overlap a small portion of a neighboring die, as illustrated in Figure 15; this field edge effect is commonly referred to as the black border effect. The term black border refers to mitigation strategies that etch a non-reflective border into the ML of the image border to prevent unwanted reflections; therefore the term black border effect is a misnomer. For the sake of clarity, the term black border effect will not be used. Instead the term field edge effect will be used (section 1.3.4).

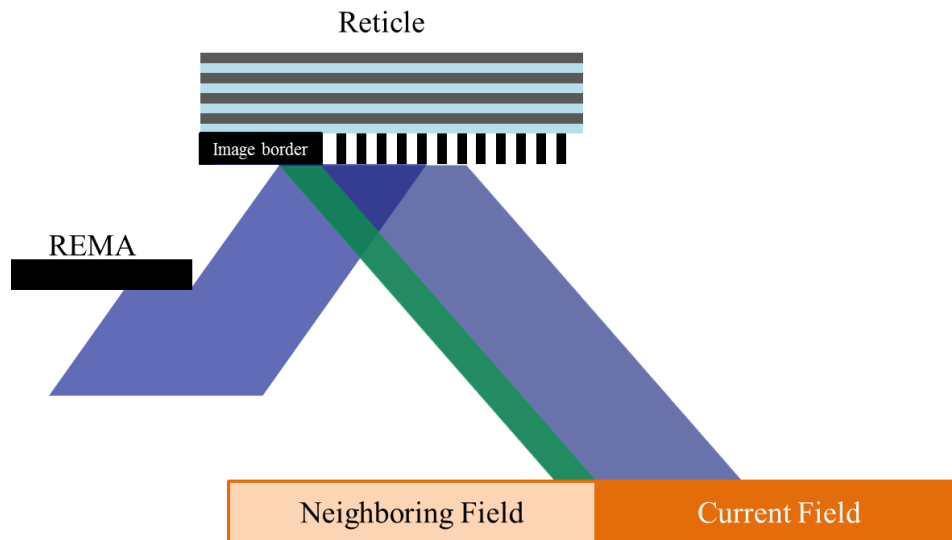


Figure 15. Illustration of image border reflections overlapping with neighboring die. These REMA blades have tolerances associated with them and are not necessarily placed in the same location every time. This changes how far the field edge effect is extended

into the neighboring field each time the REMA blades are reset. In addition the edge of the blade does not result in a clean transition between light from the source and darkness; there is a resulting penumbra (Figure 16).

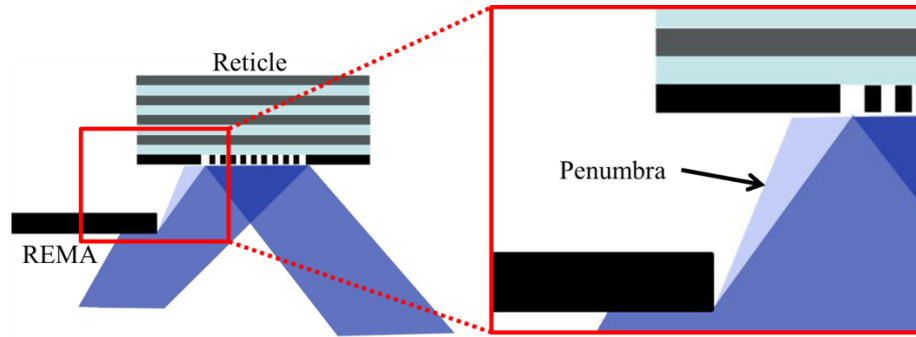
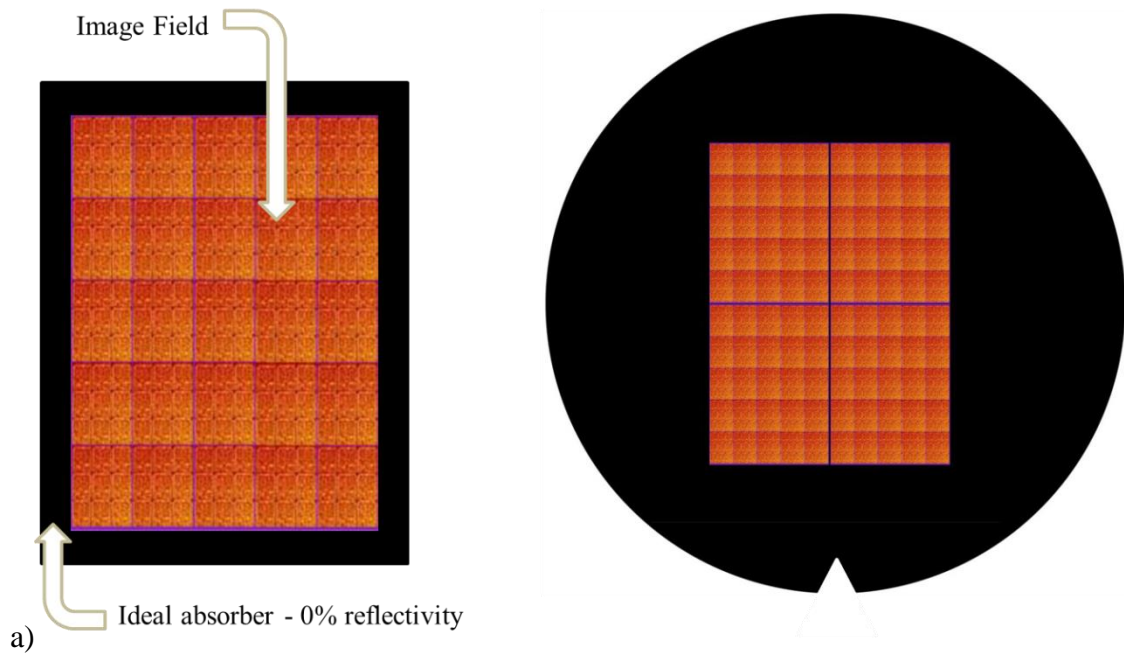


Figure 16. Illustration of REMA blade placement and resulting penumbra.

1.3.4 Field Edge Effect

One of the limiting factors in high volume manufacturing for EUVL is the field edge effect. In order for high volume manufacturing (HVM) to be realized, die must be able to be densely printed on a wafer to ensure there will be no empty wasted space, as shown in Figure 17a. Ideally, there should be no reflection of EUV light from the absorber of mask. In reality, this is not the case (Figure 17b). Since EUVL requires a non-telecentric reflective optical system for operation, many EUVL specific challenges arise. One of those challenges is shadowing. To limit shadowing, it is desirable to use a thinner absorber. As the thickness of the absorber decreases, the reflectivity in the ideally 'dark' or 'black' region around the image field increases, resulting in a loss of contrast. The region around the edge of the die on the mask of un-patterned absorber material deposited on top of ML, known as the image border, is also susceptible to undesirable

reflections in an ideally 'dark' region. For EUVL to be enabled for HVM, REMA blades are used to shield light from the image border to allow for the printing of densely spaced die. When die are printed densely, the image border of each neighboring die will overlap with the edge of a given die resulting in an increase of dose that overexposes features at the edge of the field. This phenomenon will be referred to as a field edge effect.



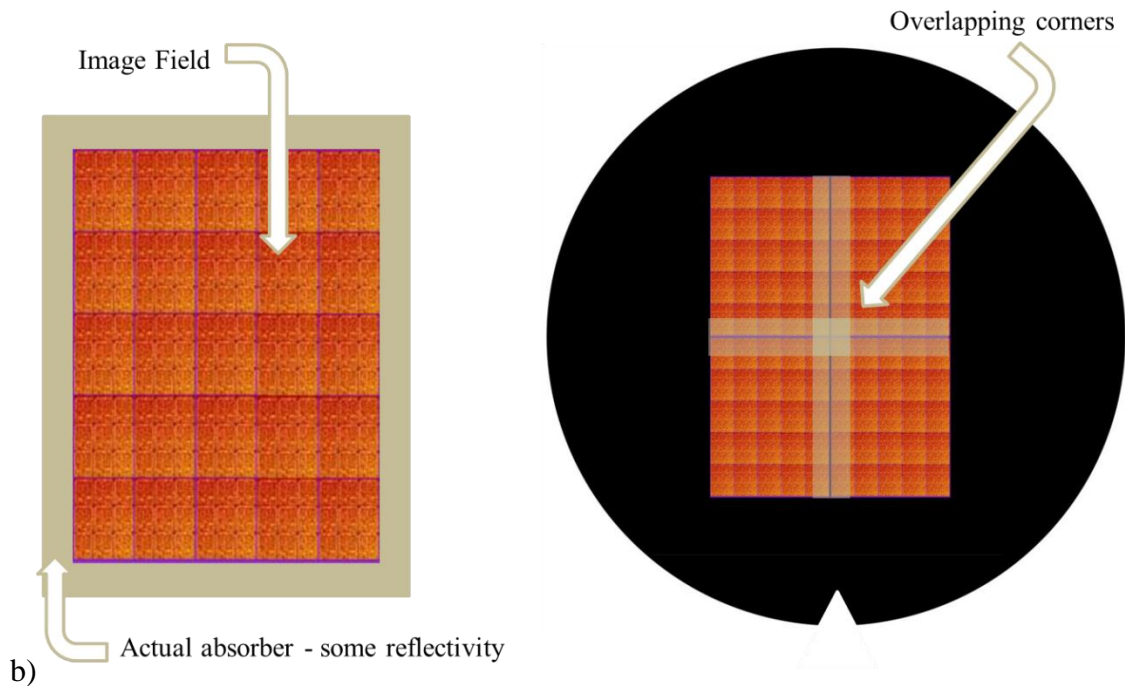


Figure 17.a) Ideal die stitching. b) Actual die stitching showing overlapping image borders overexposing the image field.

1.3.5 OoB Radiation

For certain field edge effect mitigation techniques, such as etching through the ML in the image border, actinic-EUV reflections can be prevented at mask level, but out-of-band (OoB) radiation still has a chance to reflect from the mask substrate. EUV sources are designed to emit 13.5nm actinic-EUV radiation, but they are also known to emit OoB radiation especially in the deep ultraviolet (DUV) range [36]. This OoB radiation must also pass through the complex system of 11 mirrors optimized to reflect EUV radiation, but the mirrors are also susceptible to DUV reflections (Figure 18) [37].

Enough OoB radiation reaches the wafer surface to result in a small but measurable contribution since most EUV resists are sensitive to OoB radiation.

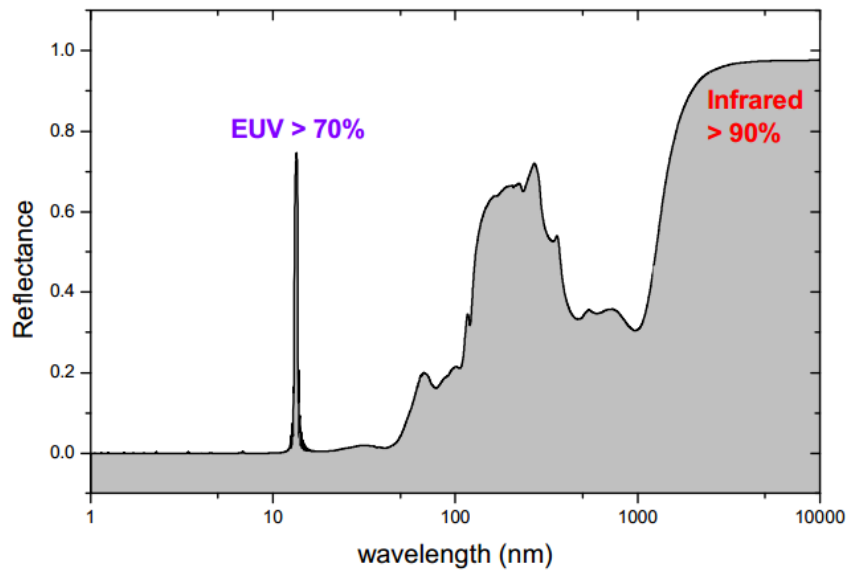


Figure 18. Theoretical reflectivity for Mo/Si ML mirrors.

1.3.6 Stochastic effects

Lithographic modeling to date has mostly used the continuum approximation which uses continuous mathematics to describe the mean-field behavior as depicted in Figure 19a [31], [38], [39].

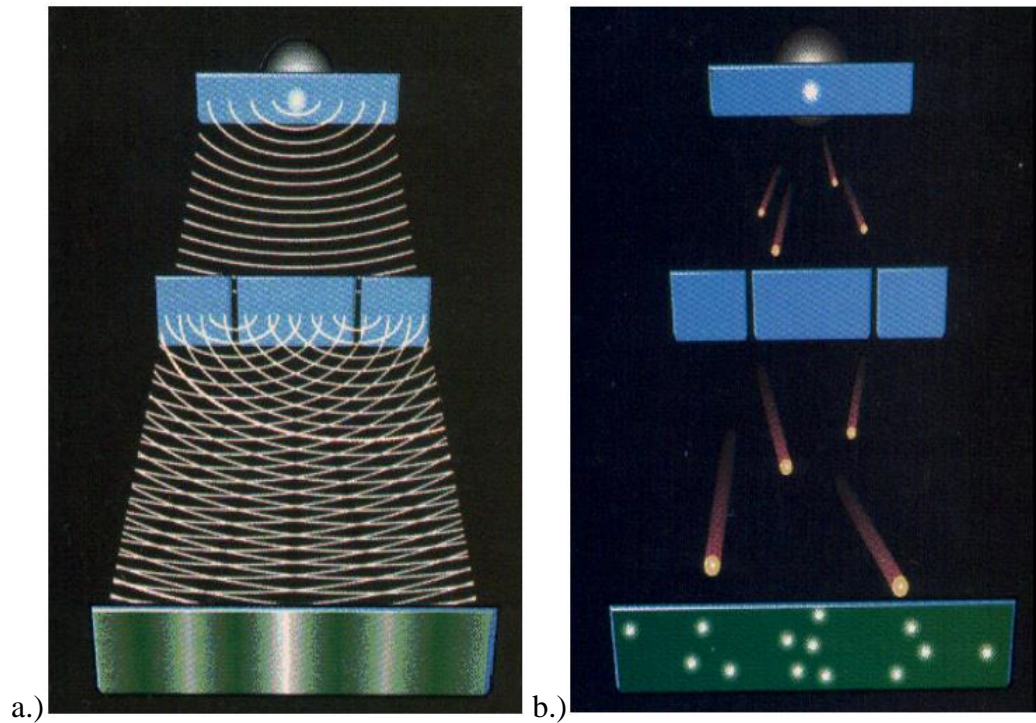


Figure 19. a.) Continuum approximation used in resist modeling. b.) Stochastic resist modeling showing photon and resist reactant randomness.

However, in EUV lithography, the resist is designed to be very sensitive as a result of the lack of source power, thus adding some randomness into the imaging. In some instances when using ultra-sensitive resists, it is no longer acceptable to use continuous simulations to analysis an image in resist. Since very few photons are being used to expose the resist, the signal to noise (SNR) ratio is quite low as expressed in Equation (16), where N is the number of photons.

$$SNR = \frac{N}{\sqrt{N}} = \sqrt{N} \quad (23)$$

If the photons are thought of as discrete particles with some small randomness associated with them it is possible to understand this concept. Think of a laser emitting many

photons with some small randomness associated with them; at the image plane, they will average together to produce the desired image. On the contrary, if only a few photons with some small randomness are emitted at a time, then the averaging will not be as clear and the randomness will be pronounced. This concept is known as shot noise [40]. In addition, the resist reactants are discrete molecules and are randomly distributed within the resist. Stochastic effects describe behaviors at the length scale of tens of nanometers by taking into account the quantization of light and matter. Prolith Stochastic Resist Modeling will be used in this work to simulate and analyze the local CD uniformity of 36nm dense contact holes as shown in Figure 20.

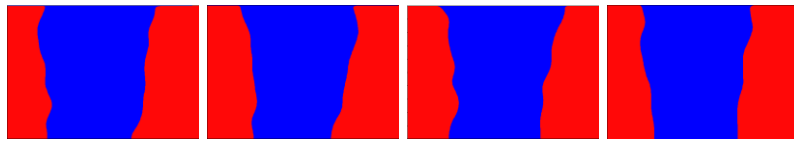


Figure 20. Four contact hole cross sections generated using Prolith Stochastic Resist Modeling (red=resist).

2. Research Motivation

2.1 Problem

As device generations continue to shrink, optical lithography solutions are continually being realized and extended. These solutions however, come with a price. Double and multiple patterning solutions [41] may be able to print at the desired technology nodes, but at the cost of multiple lithography and processing steps as well as limiting the layouts of the standard cell library [42], [43]. EUVL offers a possible solution to the problems that drive up the cost and complexity of 193i multiple patterning. For EUVL to be a viable solution it must first be enabled for HVM.

One requirement to enable HVM is to have the capability to print densely spaced die. What makes this difficult is that EUVL is constrained to use a non-telecentric reflective optical system for operation. The design of this system creates many EUVL specific challenges. 3D mask effects are one of the difficulties that can be reduced by the use of a thinner absorber, but at the cost of less absorption. One of the difficulties that arise from using a thin absorber is seen when dense die are printed; the image border of each neighboring die will overlap with the edge of a given die resulting in an increase of dose that overexposes features at the edge of the image field. The extra dose is convolved with a fingerprint from the edge of the REMA blades, and results in a field edge effect.

Mitigation strategies for field edge effects, such as an etched ML border [44], [45] can help to reduce the issue but some residual effects still remain such as OoB radiation reflecting from the mask substrate.

2.2 Objectives

This study will consist of two objectives. The first is to model the field edge effects with an absorber border and ML etched border using Mentor Graphics' Calibre software. The second is to explore the limits of OPC when compensating for field edge effects. Others have claimed that the field edge effects can simply be compensated for with OPC[46], but this approach is not trivial and will have its own unique obstacles [47]. The goal of this study is to uncover these obstacles and define what requirements exist for OPC to be used as a compensation strategy.

3. Approach

3.1 Experimental

3.1.1 ML etched mask

To enable HVM, field edge effects must be mitigated. A few strategies that are available to explore include etching the ML in the image border, implementation of a non-reflective absorber by using a complex absorber stack, thicker absorbers, the development of REMA blades with improved accuracy and repeatability and sub-micron penumbra range, OPC or some combination of these. The mitigation strategies that we will be investigating in this study are to apply OPC both to a reticle with an absorber border and also to an etched ML border. The etched ML border will surround the image field in the same manner that a moat surrounds a castle. The moat will be etched with a width of 2mm on the left and right sides of the mask and 3mm on the top and bottom. Figure 21 shows a cross section of the etched ML border, as you can see the ML is completely removed from this region, meaning no actinic-EUV light can reflect from this region. If there are any reflections in this region, they will be from OoB radiation.

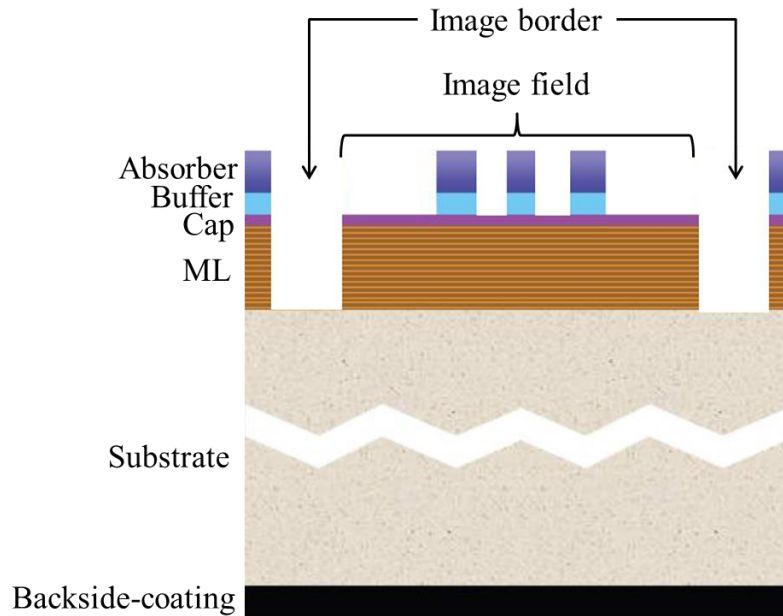


Figure 21. Cross-section of etched ML border.

3.1.2 Dense CH Array Measurements

Dense contact hole (CH) measurements will be made using a half-pitch of 36nm. This dimension was chosen for multiple reasons. First, this dimension is resolvable using a conventional partially coherent source on the ASML NXE:3100, which would maximize source power on a tool where photons are expensive. Second, this pitch is representative of features that would be found near the edge of a die or in the scribe-lane. Typically either dummy features, alignment marks or test features are imaged here, but depending on the layer, it is possible to have extra logic or memory components found here that are often used as a fail-safe for other devices. These 36nm dense CHs will be arranged in such a way where they can be measured as a function of distance from the edge of the field. To measure the field edge effect these dense CH test patterns will be placed at the edge of the field and extending inward from the top, bottom, left, right and

diagonally from the corner of the field as shown in Figure 22. The measurement positions are illustrated as black lines. Measurements will be made both on a standard mask as well as mask with and etched ML. Metrology will be completed on a Hitachi CG5000 CD-SEM.

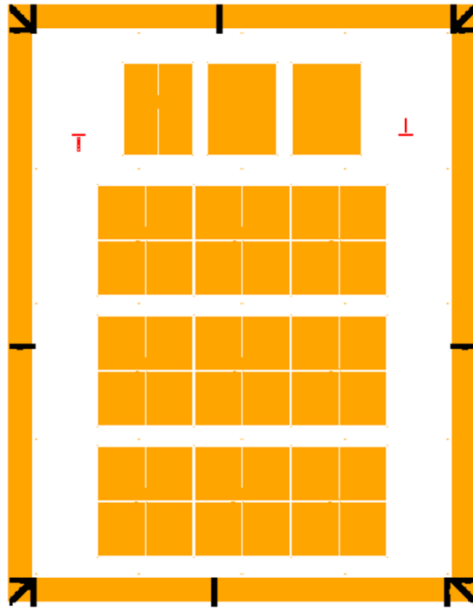


Figure 22. Reticle layout showing measurement positions of 36nm dense contact holes in black.

3.1.3 Measuring OoB variability

IMEC has developed a unique and repeatable way of measuring the contribution of OoB radiation in the NXE:3100 scanner. The process involves two mask blanks. One containing only reflective ML with no absorber and the second is a mask black coated with aluminum. The aluminum coated mask reflects almost 100% of OoB (DUV) light and does not reflect EUV light well as shown in Figure 23 and Figure 24 respectively [48].

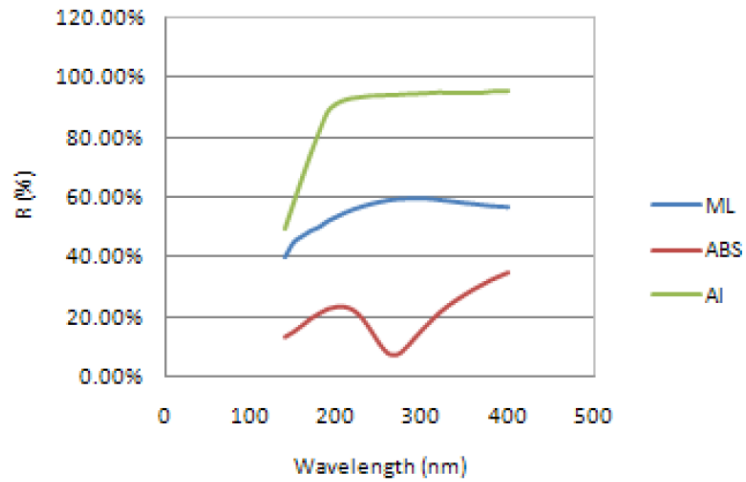


Figure 23. DUV reflectivity in multilayer, absorber and aluminum blanks.

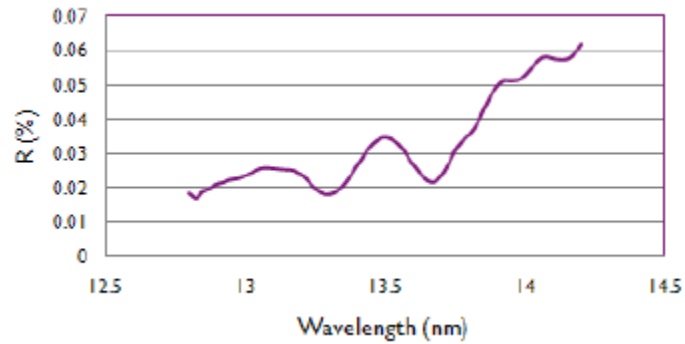


Figure 24. EUV reflectivity in aluminum.

If two wafers are now exposed, one with a ML blank and the other with the aluminum blank, it is possible to take a ratio of DUV light to EUV light to find the percentage of DUV light. This is done by finding the dose to clear for each exposure (Figure 25) [49] and calculating the ratio of dose to clear from the ML blank over the dose to clear from the aluminum blank and multiplying by 100.

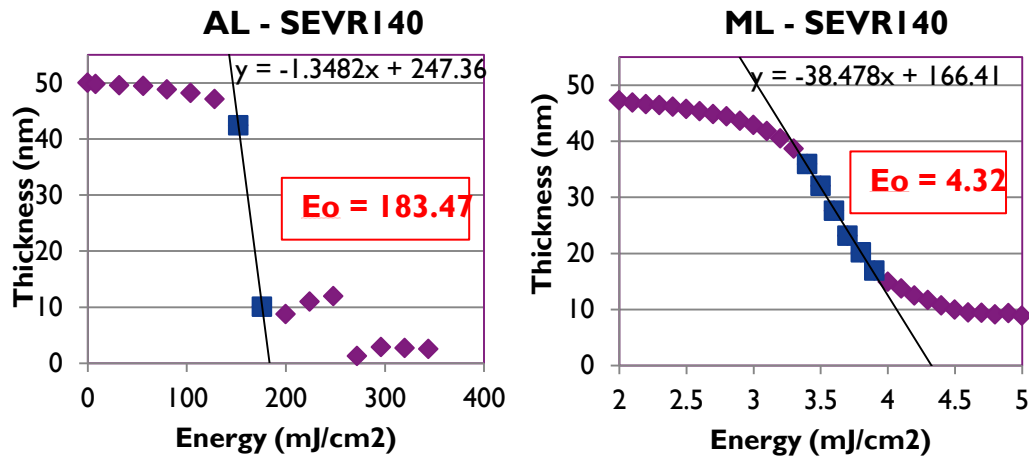


Figure 25. Dose to clear using both aluminum blank and multilayer blank.

3.2 Simulations

3.2.1 Field edge effect model fitting

In previous work, optical and resist models have been calibrated for contact holes to account for both shadowing and flare effects [50]. This model was targeted towards 27nm dense CHs; 36nm dense CHs were included in the verification sample set. Using the measurements of the contact holes as a function of distance from the edge of the field, Mentor Graphics' Calibre software can be used to generate flare maps that include field edge effects, as shown in Figure 26. Using this software, it is fairly straightforward to add a constant ring of dose around the edge of the flaremap and also to add a linear roll-off to represent the REMA blade penumbra. To add these values, one must first optimize the amount of dose around the edge using the measurement data. Next, the REMA blade roll-off can be modeled just by implementing a simple linear term. These values should be optimized for all edges to successfully predict the field edge effect in the corner of the die

where the additional dose is the most extreme. Flaremaps will be generated and optimized for both the standard mask as well as the ML etched mask.

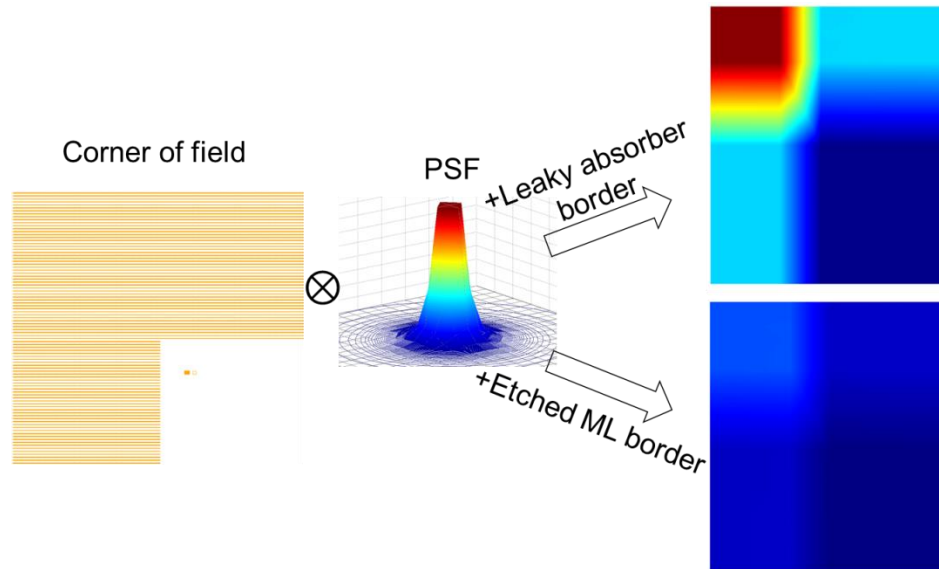


Figure 26. Flaremap generation for field edge effects.

3.2.2 OPC

There have been previous studies to show how EDA software can model the field edge effect and it has been assumed that since the effect can be modeled, OPC can be used to compensate for it [46]. This may be true, but there have also been publications showing poor OPC results based on this assumption[47]. The issues behind these results have yet to be investigated further. Using the calibrated optical and resist models as well as the optimized flaremaps, OPC will be completed using Mentor Graphics' nmOPC software to compensate for the field edge effect in the corners of the die. The corners of the field will be the focus for this study since they represent the worst-case scenario. In EUV, SRAFs have not been implemented for OPC yet therefore only biasing will be used

to compensate for the field edge effect. As a result of shadowing, biasing will be unequal in the x and y directions. In addition, OPC will account for pattern shift that is caused by inequalities in + and – diffraction orders, also a result of shadowing. An example of how a 36nm dense contact hole array is corrected for using OPC can be seen in Figure 27. This result was found by moving the edges in and out and evaluating the aerial image at each position until convergence on the best solution.

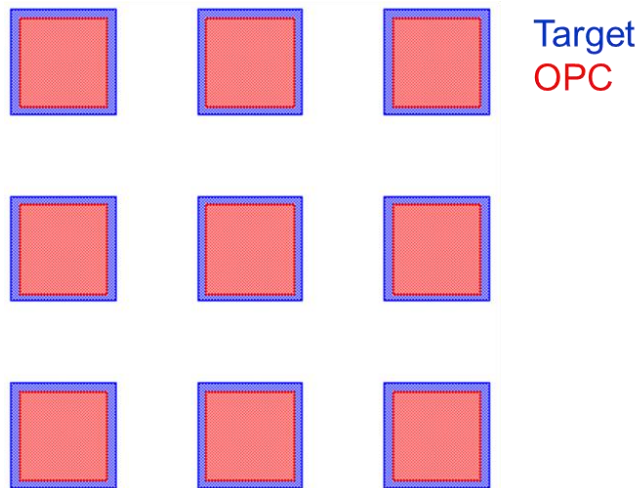


Figure 27. Example of how OPC will be used to correct 36nm dense contact holes.

3.2.3 Image Quality

Once the OPC has been completed, all features will print to the 36nm specified target dimension. Two features in particular will be compared to analyze image quality. The inner most CH array, which should see no effect from field edges and the CH array that is most effected by the field edge effect will be compared to evaluate how robust the image quality is at either location. It is predicted that NILS will decrease towards the edge of the field since there will be extra dose closer to the edge. This extra dose should

behave the same way that flare does and should decrease the amplitude of all diffraction orders except for the 0-order. It is expected that the image modulation should decrease as well as the depth of focus. What will be important to note is the extent to which image modulation and depth of focus are altered by the field edge effect. If the image quality is too poor for OPC to compensate for the field edge effect then it can be concluded that another mitigation technique such as etching the ML border is a necessity. In addition, stochastic effects will be taken into account using Prolith Stochastic Resist Modeling to analyze the local CD uniformity. It will be of interest to see how features seeing the field edge effect that are corrected with OPC compare to features at the center of the field.

3.2.4 REMA Blade Positioning after OPC

One feature that can be modified in the flaremap generation is the REMA blade placement. It is planned to carry out the OPC with the REMA blades placed in the location that the measurements were taken at, this will be the nominal position. Additional flaremaps will be generated at various REMA blade positions to evaluate the effect that REMA blade positioning errors will have on the CDs for the CHs that have been OPC'd for the nominal location of the REMA blades. Figure 28 shows how the REMA blade could end up in different locations each time it is reset, where the red line shows the nominal position. There is some tolerance associated with the REMA blade tolerance and by simulation we can determine how strict the spec for this tolerance must be.

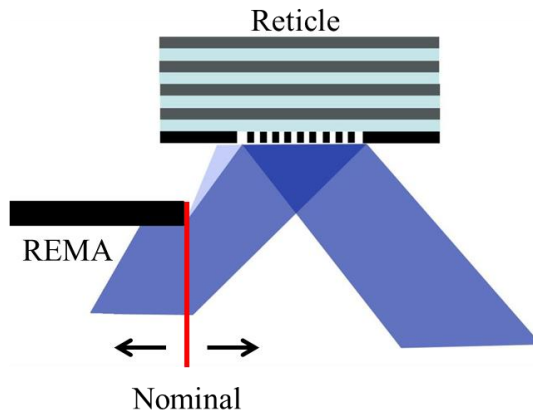


Figure 28. Illustration of how the REMA blade may vary from its nominal position.

3.2.5 Simulating OoB variability

Adding the OoB contribution to the flaremap can be not trivial. First, for the sake of simplicity, this will only be done for the ML etched border scenario. In this case, if there are any field edge effects then they will be assumed to be a result of OoB radiation.. For this, the value that is converged on through flaremap optimization to provide the extra ring of dose represents our OoB contribution in terms of residual EUV reflectivity ($EUV_{calibrated}$). If the OoB contribution is known ($OoB_{measured}$) then a simple ratio can be used to give an estimation of how the resist would respond to different OoB levels ($OoB_{desired}$). Knowing this ratio, it is then possible to control the amount of OoB in the simulations by using this ratio to calculate the input value (EUV_{input}) for flaremap generation for a desired OoB percentage, as shown in Equation (24).

$$\frac{EUV_{calibrated}}{OoB_{measured}} = \frac{EUV_{input}}{OoB_{desired}} \quad (24)$$

Knowing the OoB variability range, it is then possible to apply OPC at the condition for the center of the range and then vary the OoB while generating subsequent flaremaps. It will be of interest to study how the CD varies for different levels of OoB and see what the CD variation is at the minimum and maximum OoB percentages.

4. Results

4.1 CH measurements

Both the standard mask and ML etched mask have been fabricated with the arrays of CHs that were previously described using a 70nm Hoya absorber. In addition, wafers with 60nm of SEVR-165 photoresist have been exposed on the NXE:3100 and measurements have been made at the field edges as well as the corners. Figure 29 shows the results for all four corners of the field, there is about a 25% CD variation between the field center and corner due to the field edge effect. These results also depict slight asymmetries between the REMA blades, adding complexity to the modeling. The asymmetries seen here are a result of two factors, the first being the REMA blade placement accuracy and the second being the non-telecentricity at the mask plane. As seen in the data, the measured asymmetries between the left and right edges exceed the expected REMA placement error. The residual discrepancy seen here can be attributed to the 6° incidence angle affecting the behavior of the REMA blade penumbra differently at the left and right edges

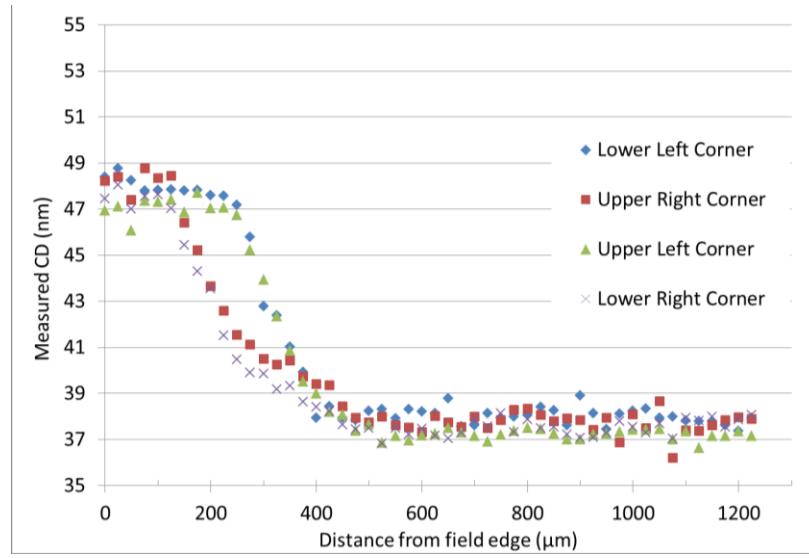


Figure 29. 36nm dense contact holes measured at distances extending diagonally from the corner of the image field.

Exposures were also made with the ML-etched border mask as seen in Figure 30. Here the CD variation is greatly reduced down to about 1nm, which is assumed to be caused by OoB radiation reflecting off of the top surface of the mask substrate. Since there is still a slight CD variation, OPC will still be required in combination with the etched ML border. It should also be noted that there is slight CD shift in CHs at the center of the field compared to the reticle without an etched ML border. This is attributed to tool drift since exposures were made on different days. Although this seems to suppress the field edge effect, using an etched ML border reticle adds complexity in an industrial setting. The ML etch must first be evaluated to show that defects are not added to the mask, and also the mask must be able to be cleaned using a standard process that does not compromise the integrity of the etch.

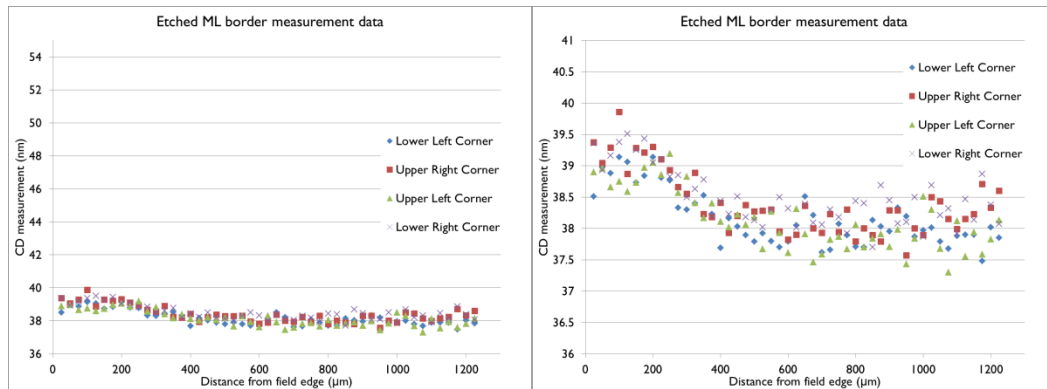


Figure 30. 36nm dense contact holes measured at distances extending diagonally from the corner of the image field using a reticle with an etched ML border.

4.2 Modeling

4.2.1 70nm thick absorbers

To model the CH measurement from the 70nm Hoya absorber, the parameters that are used to modify the constant ring of dose around the field edge and the linear roll-off parameter to model the REMA blade penumbra were calibrated. After calibration, the simulated CDs matched the measured with an RMS error of 0.475nm as shown in Figure 31.

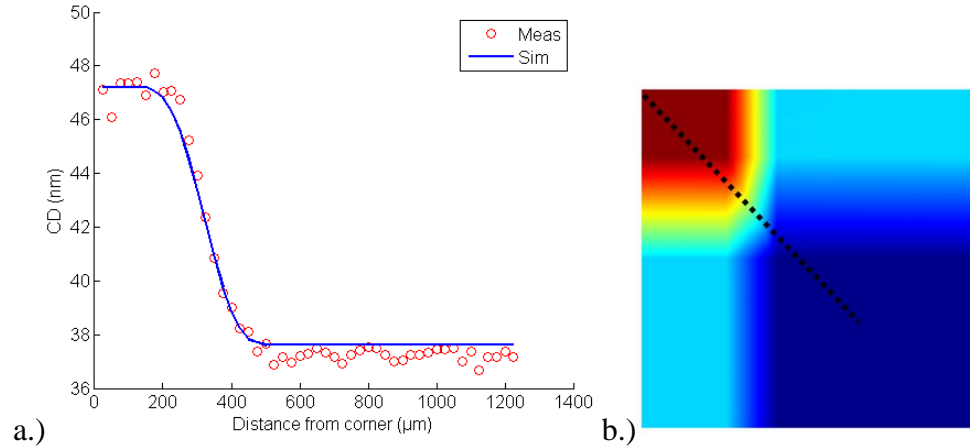


Figure 31. a.)Field edge effects from 70nm Hoya absorber at corner of the field modeled to fit measurement data. b.) Calibrated flaremap showing measurement points in black.

The modeling seen here assumes only EUV radiation is present at the field edge. In reality, there is actually EUV and some portion of DUV radiation reflecting from the border region. This will need to be addressed when extrapolating the model to different absorbers.

4.2.2 Etched ML border

The same type of model can be calibrated for a reticle with an etched ML border. In this case, the calibrated values to model the REMA blade penumbra do not need to change from the previous case. The only value that needs to be calibrated is the extra dose provided around the edge of the layout that affects the total CD shift. It is assumed that the CD variation near the field edge is caused by OoB radiation reflecting from the substrate. The Mentor Graphics software does not model OoB radiation, but we can still model the measurement results by treating it as residual EUV radiation. This results in a close fit to measurement values (Figure 32), and it would then be possible to vary the

OoB percentage by taking a ratio of the measured OoB for the measurement points and taking a ratio of OoB to the calibrated residual EUV radiation.

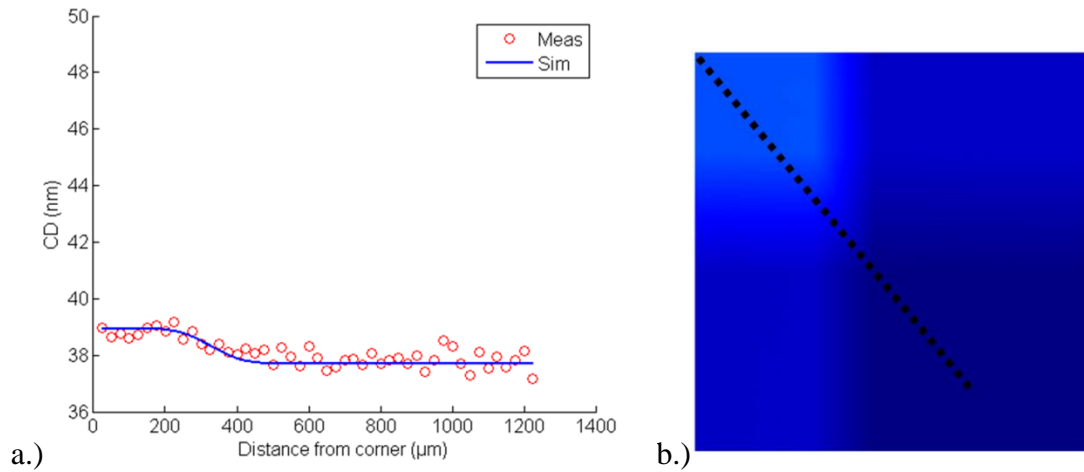


Figure 32. a.)Field edge effects from etched ML border at corner of the field modeled to fit measurement data. b.) Calibrated flaremap showing measurement points in black.

4.2.3 Extrapolating to 51nm and 84nm absorbers

To extrapolate the modeling results to different absorbers, both the EUV and DUV reflectivity must be known. What is desired when extrapolating to different absorbers is the expected CD shift. The EUV absorber reflectivity for each absorber at 6° incidence was simulated as shown in Figure 33 using Sentarus-Litho EUV.

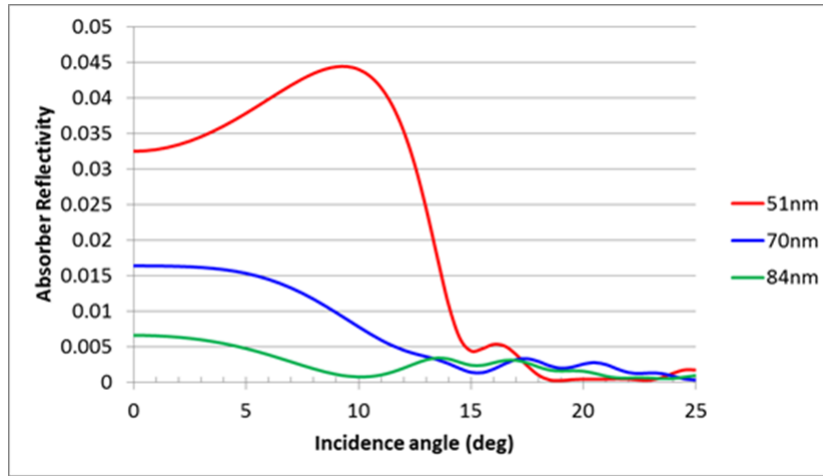


Figure 33. EUV absorber reflectivity for three different absorber types.

It is assumed that the ML etched border has a negligible amount of EUV reflectivity. It is not trivial to specify the amount of DUV reflectivity in the border region. The photoresist is sensitive to DUV wavelengths, but the sensitivity varies throughout entire spectrum. The amount of DUV reflectivity from the absorber also varies throughout the spectrum. From Figure 23, an average value of 15% for all absorbers will be used for the extrapolation to simplify the calculation. From measurements, the etched ML DUV reflectivity is about 6%. These approximations are also consistent with values used in similar studies [51].

Border type	EUV Reflectivity	DUV Reflectivity
51nm Hoya absorber	3.98%	15%
70nm Hoya absorber	1.45%	15%
84nm AGC absorber	0.35%	15%
Etched ML	0%	6%

Table 1. EUV and DUV reflectivity at 6° for four different border types.

This makes the assumption that the percentage of reflectivity through the entire spectrum is constant, which is not true, but will give an approximate value of expected CD shift. Using the 70nm absorber and etched ML cases, one can estimate the EUV and DUV sensitivities in terms of nm per percent of reflectivity. These sensitivities can then be used to give an approximation of CD shift for different absorbers.

First, to determine the DUV sensitivity (in units of nm per percent of ML reflectivity), the etched ML case will be evaluated with three overlapping fields resulting in a 1.2nm CD shift.

$$3(6\% * DUV_{sens}) = 1.2nm \quad (25)$$

$$DUV_{sens} = 0.067 \frac{nm}{\%} \quad (26)$$

Assuming EUV reflectivity is negligible for the etched ML case, the DUV sensitivity can easily be solved for. Using this value in the 70nm absorber border case with three overlapping fields, the EUV sensitivity can then be solved for.

$$3(1.45\% * EUV_{sens} + 15\% * DUV_{sens}) = 9.5nm \quad (27)$$

$$EUV_{sens} = 1.49 \frac{nm}{\%} \quad (28)$$

Using these values along with the corresponding EUV and DUV reflectivity, this model can now be extrapolated to different absorbers. The expected CD shifts from a 51nm Hoya and 84nm AGC absorbers are calculated in Equations (29) and (30) respectively.

$$3(3.98\% * EUV_{sens} + 15\% * DUV_{sens}) = 20.8nm \quad (29)$$

$$3(0.35\% * EUV_{sens} + 15\% * DUV_{sens}) = 4.6nm \quad (30)$$

By extrapolating the model to different absorbers, the field edge effect for three overlapping borders in the corner of the field can be predicted for each case as seen in Figure 34.

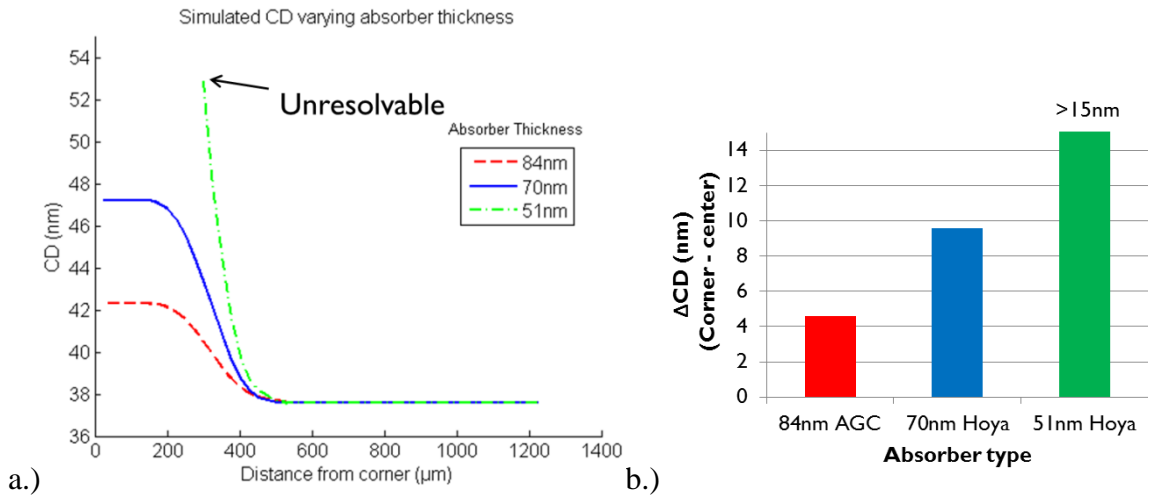


Figure 34. a.) Model extrapolated to three different absorber types. b.) Simulated CD comparison between features in the center of the field features at the corner of the field.

Investigating three different absorbers, 51nm Hoya, 70nm Hoya and 84nm Asahi Glass (AGC) it is possible to determine the best strategy for field edge effect compensation for each case. For the 51nm Hoya absorber, the 36nm dense CH features become unresolvable. This is consistent with similar experimental results but for lines and spaces [51]. As shown, the 84nm AGC absorber suppresses the CD variation significantly but will still be worse than the etched ML border solution. It can be concluded that the model

can predict the field edge effect for different absorber types using an approximation for the expected CD shift.

4.2.4 OPC

For this study, OPC will be used to provide simple biasing for the design correction of CHs. The results seen here are from a dark field mask, therefore to compensate for additional dose, the design of the contact holes must shrink. Also, since the extra dose from the field edge effect is lumped into the flaremap, it is relevant to discuss how the CD bias applied from the OPC is a function of flare. As shown in Figure 35, as flare increases, the magnitude of the required CD bias also increases.

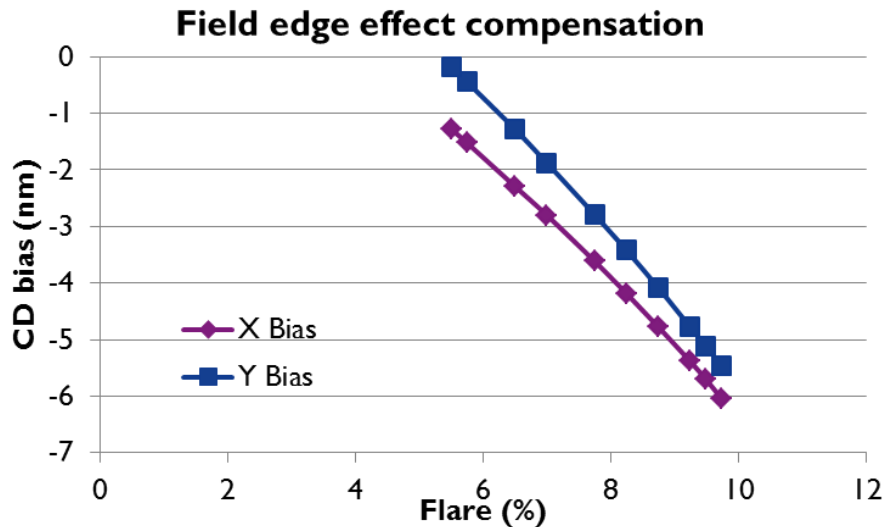


Figure 35. CD bias after applying OPC as a function of flare (field edge effects are lumped into flare).

The difference in the X and Y bias is a result of shadowing, since a 3D mask model is being used to apply the OPC. Comparing the bias required for a 70nm Hoya

absorber border and the etched ML border (Figure 36), there is a large difference in the bias required to match the printed target CD.

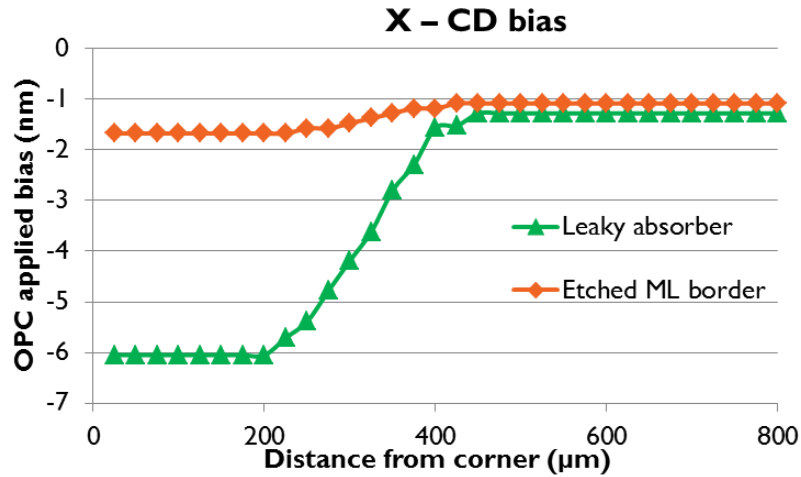


Figure 36. CD bias after applying OPC for a 70nm absorber border and an etched ML border.

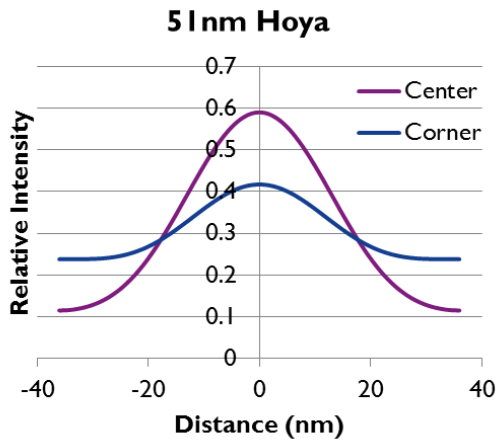
For the etched ML border, less than 2nm of bias is required, and is a fairly standard amount of bias that is typically seen for OPC. For the absorber border case, about 6nm of bias is required; now this raises some questions. 6nm of CD bias is quite large, so one must investigate how the need for such a large correction impacts the image quality of the contact holes. OPC was also applied to the 51nm Hoya and 84nm AGC absorbers.

4.3 Requirements for design correction

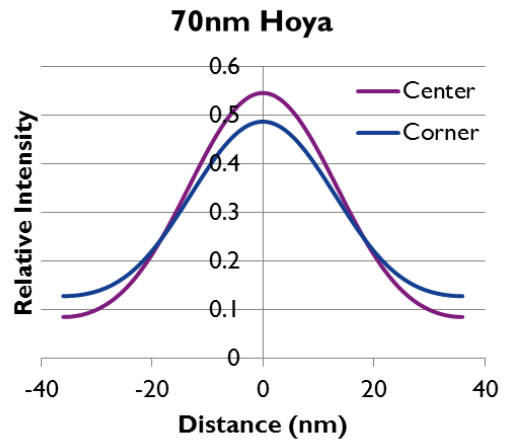
4.3.1 Good image quality

4.3.1.1 Aerial image

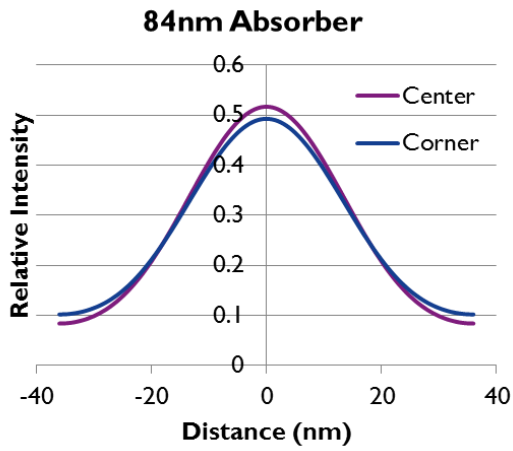
The first domain that will be evaluated for image quality will be the aerial image. After OPC is applied, 36nm dense CHs at the center of the field will be compared to the worst case scenario of 36nm dense CHs at the corner of the field seeing field edge effects from three overlapping neighboring fields. A calibrated Prolith resist model and 3D mask models are used for the image quality analysis. The source conditions for this simulation correspond to the measurements made on the NXE:3100 with an NA of 0.25 using conventional illumination with a σ of 0.81. By changing the optical constants of the mask and the material thickness, different absorber types can be used in Prolith. The field edge effect will be lumped into the DC flare level the same way that it was using the Mentor Graphics software. For each absorber type, the aerial image was computed after OPC for features at the center of the field and those most influenced by the field edge effect located at the corner of the field (Figure 37). The NILS for each case is calculated as shown in Figure 38. For the 70nm Hoya and the 84nm AGC absorber the contrast degrades and therefore NILS, but NILS is still greater than 2, giving an indication that the image quality should be reasonable if OPC is going to be used to correct for field edge effects. The 51nm Hoya absorber shows a large degradation in contrast, resulting in NILS less than 1 for an OPC corrected feature at the corner of the field. From this, it is possible to predict that for a 51nm Hoya absorber, using only OPC to compensate for field edge effects may not be a reasonable solution and some additional mitigation strategy (such as etched ML border) would be required.



a.)



b.)



c.)

Figure 37. Aerial image comparison between 36nm dense CHs at the center of the field vs. features at the corner of the field for three different absorbers a.) 51nm Hoya b.) 70nm Hoya c.) 84nm AGC.

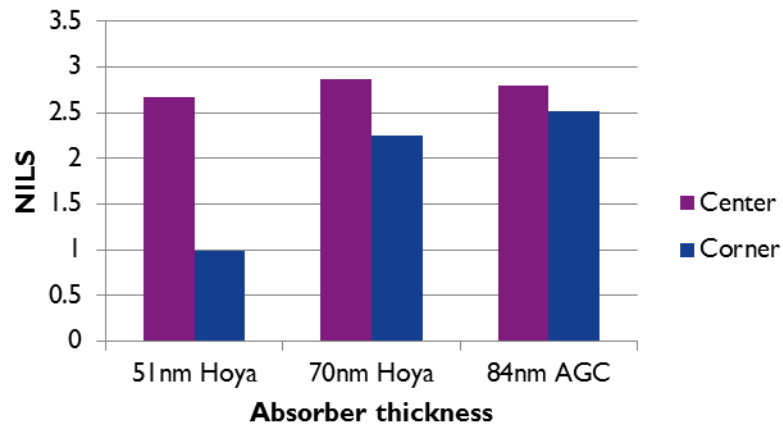
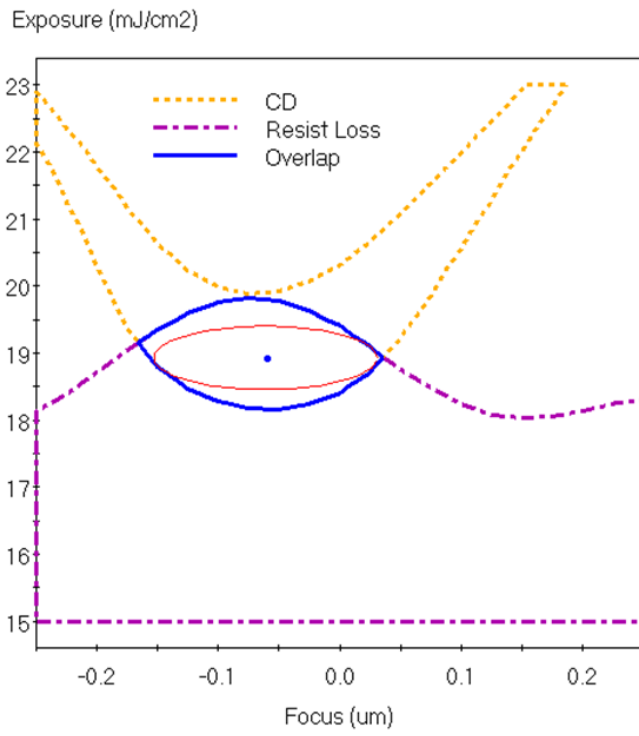


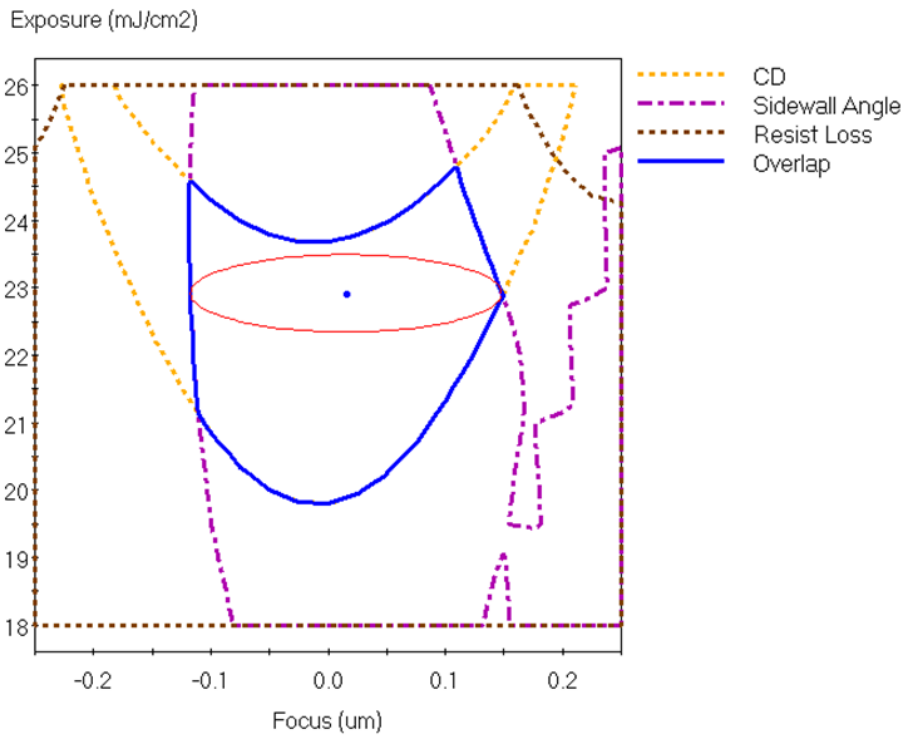
Figure 38. NILS corresponding to the simulated aerial image for 36nm dense CHs at the center of the field and features at the corner of the field after OPC corresponding to three different absorbers.

4.3.1.2 Process window

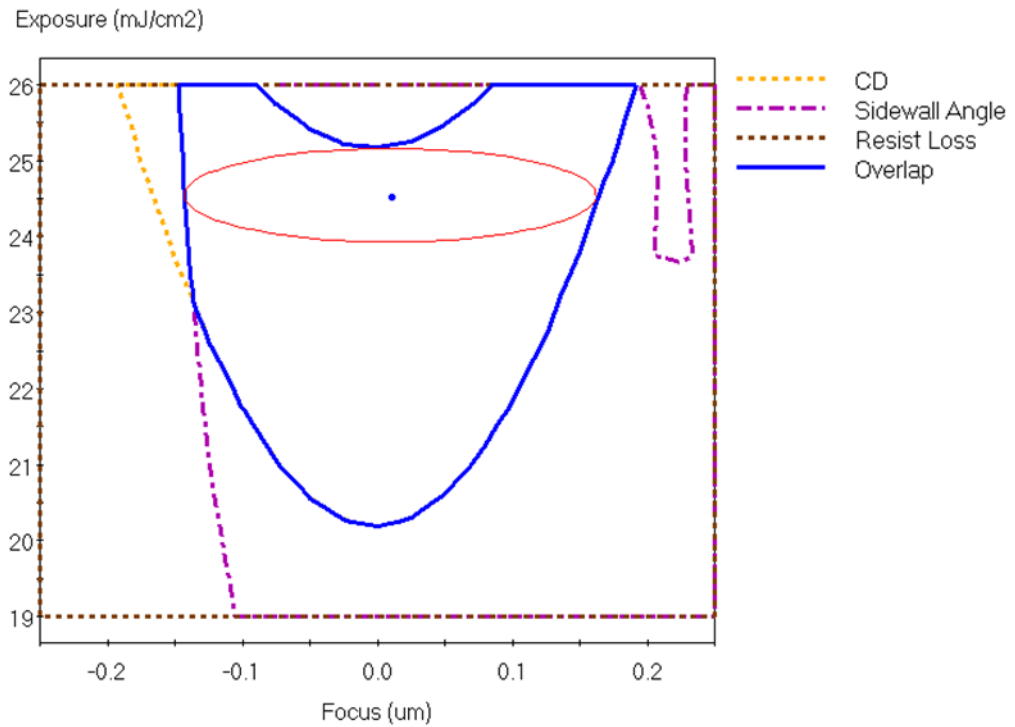
To analyze the imaging quality through process window, one must first decide which metric will be used to define the acceptable tolerance. For 36nm dense contact holes, the main quantity that will be compared will be depth of focus at 10% exposure latitude. The minimum acceptable depth of focus for this study is 100nm. To analyze the process window, a focus exposure matrix was simulated in Prolith using a calibrated resist model and a 3D mask model. Figure 39 illustrates the simulated process window that is available for features in the corner of the field after OPC.



a.)



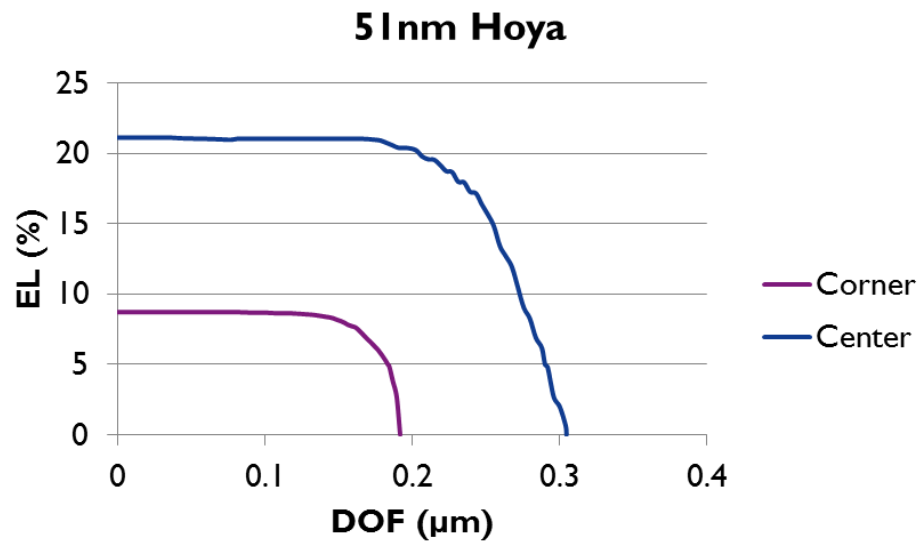
b.)



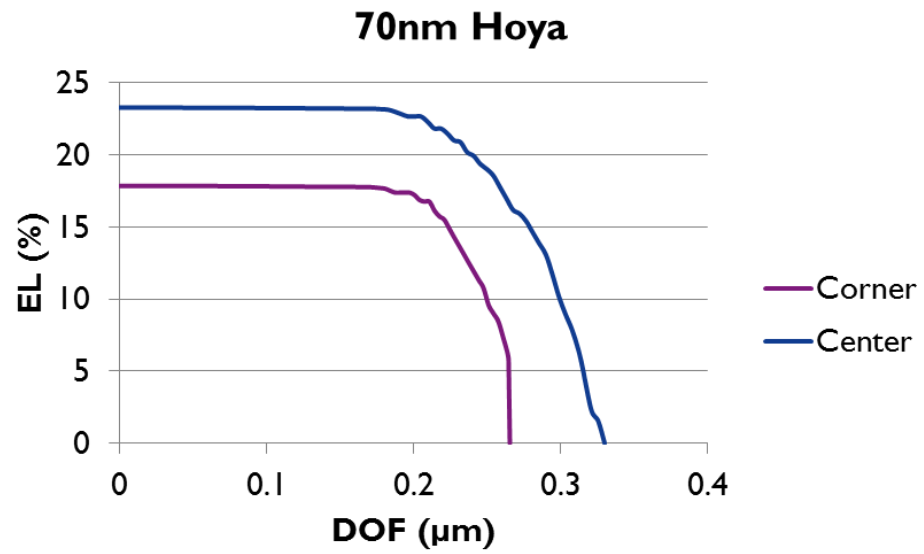
c.)

Figure 39. Simulated 36nm dense CH process window for features in the corner of the field seeing the effects of three overlapping fields after OPC a.) 51nm Hoya absorber b.) 70nm Hoya absorber c.) 84nm AGC absorber

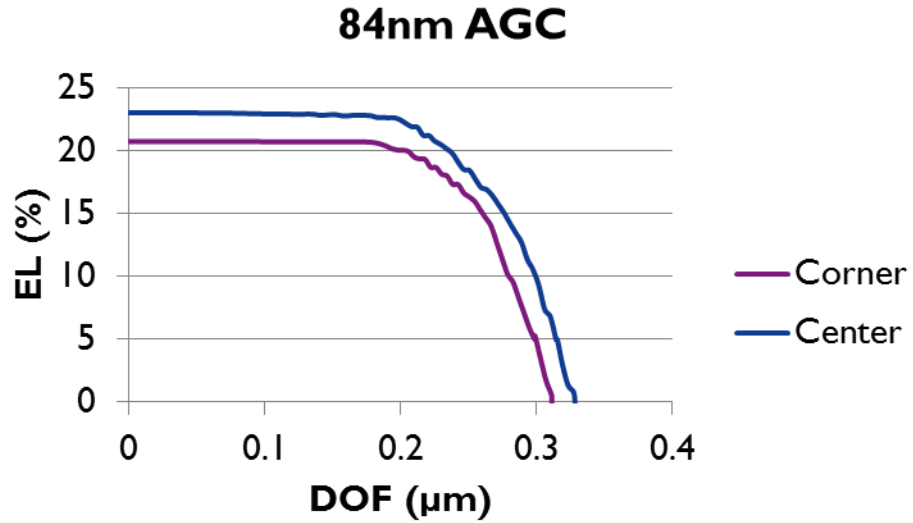
For the 51nm Hoya reticle, the sidewall angle constraint was not included in the analysis for the sake of discussion since it originally resulted in no available process window. From these plots, it is possible to extract the best focus and dose condition for the features, but it gives more a qualitative description of the actual process window. In an attempt to better quantify the results, the depth of focus for different exposure latitudes was plotted. Now it is possible to extract the maximum EL and DOF values as well as the DOF at 10% exposure latitude. Figure 40 shows how each reticle behaves differently when features in the corner of the field are corrected for using OPC.



a.)



b.)



c.)

Figure 40. Simulated 36nm dense CH exposure latitude vs. depth of focus curves for features in the corner of the field seeing the effects of three overlapping fields after OPC a.) 51nm Hoya absorber b.) 70nm Hoya absorber c.) 84nm AGC absorber

Comparing these results with features in the center of the field, there is degradation in exposure latitude and depth of focus. The degree of degradation is what makes each case unique. For the 51nm Hoya absorber, there is more reflection from the border region resulting in less contrast and therefore reducing the process window below the 100nm DOF requirement at 10% EL. This proves that OPC cannot correct for field edge effects for the 51nm Hoya absorber; there must be an additional mitigation strategy such as the etched ML border. For the 70nm Hoya absorber there is degradation in exposure latitude and depth of focus and about a 50nm loss in depth of focus at 10% exposure latitude. This still meets the process window requirement, so in terms of contrast and process window, it would be acceptable for a 70nm Hoya absorber border to be corrected for with OPC. The same is true for the 84nm AGC absorber, there is only a 22nm degradation in depth of focus at 10% exposure latitude. The quantitative process

window results after OPC at the center and at the corner of the field have been summarized in Table 2.

Absorber type	Field Location	Max EL	Max DOF	DOF @ 10% EL
51nm Hoya	Center	21.1%	305nm	272nm
	Corner	8.7%	192nm	0nm
70nm Hoya	Center	23.3%	330nm	300nm
	Corner	17.8%	266nm	250nm
84nm AGC	Center	23.0%	328nm	300nm
	Corner	20.7%	311nm	278nm

Table 2. Simulated 36nm dense CH process window results after correcting with OPC for field edge effects.

4.3.1.3 Stochastic effect on LCDU

Since EUV is currently struggling with low source power, photoresists have been developed to be very sensitive. This enables good contrast with only a minimal amount of photons. The drawback of having such high sensitivity photoresist is that it begins to show properties of a stochastic system. When using only a minimal amount of photons to expose the resist, they all might not land in the desired location to generate the proper image; this is known as photon shot noise. To investigate the stochastic effects on the local CD uniformity (LCDU), a random variable in Prolith was turned on to enable stochastic effects and the CD in the resist was simulated 50 times for each contact hole. This includes all three absorbers, at the center and at the corner of the field after OPC. It is predicted that features in the corner of the field will show enhanced roughness and more local variability in the field corner due to a decrease in contrast. The results of the simulations can be seen in Figure 41 and summarized in Table 3.

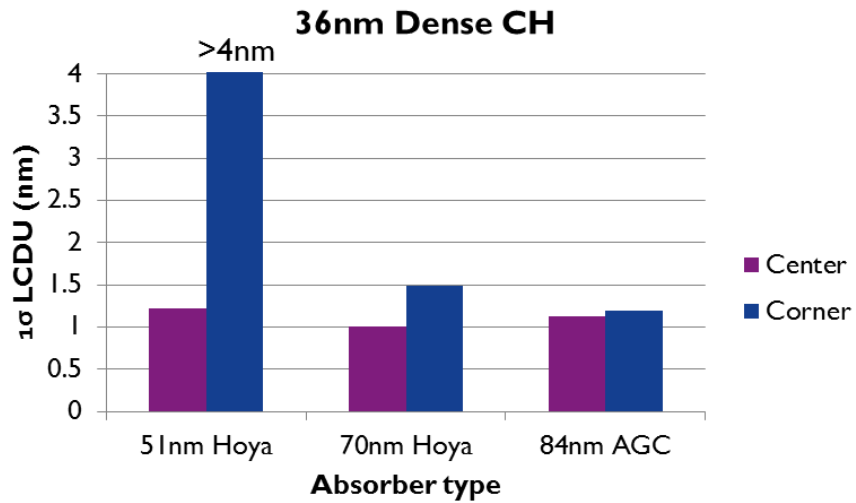


Figure 41. Simulated LCDU for 36nm dense CHs in the center of the field and in the corner of the field after OPC.

Absorber type	$\Delta 1\sigma$ LCDU
51nm Hoya	>4nm
70nm Hoya	0.48nm
84nm AGC	0.07nm

Table 3. Simulated 36nm dense CH process window results after correcting with OPC for field edge effects.

As expected, the 51nm Hoya absorber shows high LCDU for features in the corner of the field. This is due to low aerial image contrast forming a wider distribution for the photons to land, resulting in high variability. For the 70nm Hoya absorber, an increase of 1σ LCDU of 0.48nm might not seem like a large impact, but looking at this in terms of 3σ variability, it actually increases about 1.5nm. Having such a large variability does not support an OPC only solution to compensate for field edge effects for the 70nm Hoya absorber. On the contrary, the 84nm AGC absorber suppresses stochastic effects on LCDU for features in the corner of the field. There is a slight degradation of 0.07nm 1σ

LCDU, but this would be acceptable for the application of OPC to compensate for field edge effects. The degradation due to stochastic effects all stem from aerial image contrast. As contrast decreases, the distribution that we would expect to see photons widens and therefore results in more variability.

4.3.2 Stable REMA blade position

With the ability to simulate multiple REMA blade positions it is possible to investigate the effect that the REMA blade positioning error would have on OPC. The first thing to note is that if the accuracy value is known, it can be calibrated for, so the only error that would be left over will be from the precision of the REMA blades. So if the 36nm dense contact holes are corrected for with OPC at the center of the distribution, this will give the best performance when taking into account REMA blade positioning errors. Table 4 shows examples of moving the REMA blades in and out 50 μ m for the 70nm Hoya absorber case as well as the etched ML border case with the flaremaps generated for each case on the same scale.

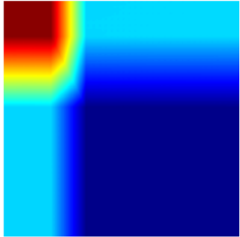
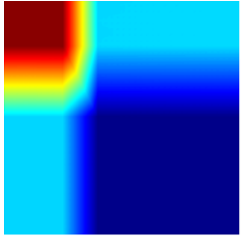
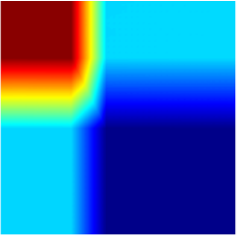
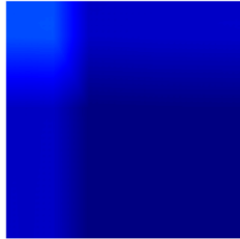
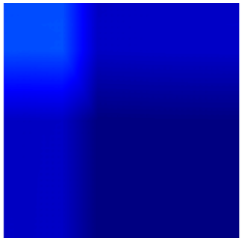
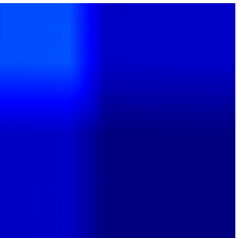
	Relative position		
	-50 μm	Nominal	+50 μm
Leaky absorber border			
Etched ML border			

Table 4. Flaremaps generated for multiple REMA blade positions.

After generating a library of flaremaps, it is now possible to see how the CDs of 36nm dense CHs would respond to different REMA blade settings before OPC is applied. Figure 42 shows simulated CDs corresponding to the cases shown in Table 4 without any OPC applied.

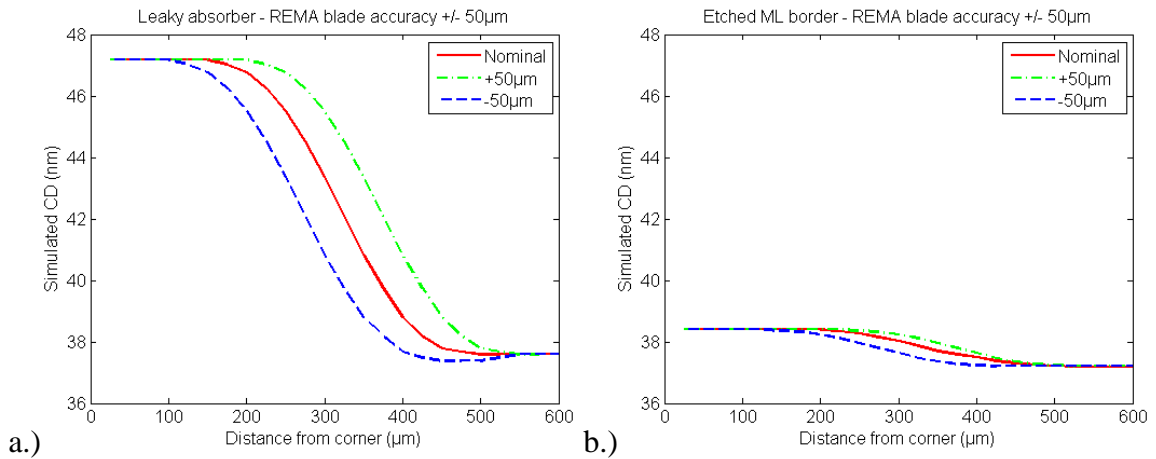


Figure 42. Simulated CD for 36nm dense CHs for different REMA blade positions before OPC a.)70nm Hoya absorber border b.) Etched ML border.

For the 70nm Hoya absorber, changing the REMA blade position has a large impact on the CD, where the simulated CD curve shifts laterally left and right. It is not an exact lateral translation since there is an artifact of the point spread function of the scanner present as shown in Figure 42a the -50µm REMA blade position shows a dip in the CD at a location of 450µm from the corner of the field. The effect of the point spread function on flare is reduced at the edge of the field due to the less superposition from the convolution of the layout and point spread function at the edges of the field. Figure 42b shows the results of shifting the REMA blades for an etched ML border. In this case, there is much less variability and therefore it is possible to predict that REMA blade positioning errors will have less of an impact on the OPC for the etched ML border case.

If the OPC is applied at the center of the REMA blade precision distribution and then the REMA blade changes position, the CD error can be simulated to show the expected error for the conditions measured at IMEC. This was done for three cases 70nm Hoya absorber, 84nm AGC absorber and the etched ML border. For OPC to be a

plausible solution, it must have a simulated CD error of <1%. The results of this simulation can be seen in Figure 43.

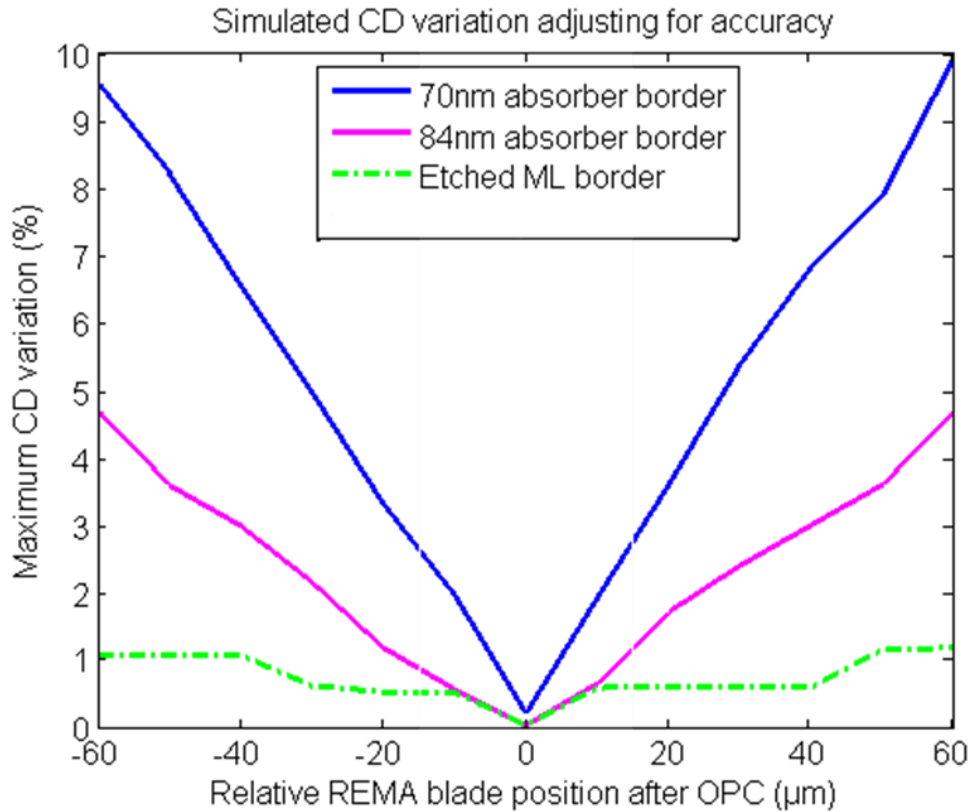


Figure 43. Simulated CD variation for different borders when shifting the REMA blade after correcting with OPC at the nominal REMA blade position.

The axis labeled ‘Maximum CD variation’ refers to the maximum CD variation simulated for all measurement points from the center of the field to the corner of the field. For the 70nm absorber, the simulated CD error reaches 1% with a REMA blade position error of +/- 5μ. In order for OPC to be a viable correction technique for the 70nm absorber, the REMA blade precision spec must be <5μm, otherwise a mitigation strategy such as an etched ML border is required. For the 84nm absorber, the simulated CD error reaches 1% with a REMA blade position error of +/- 15μm. The 84nm absorber border would be able

to support an OPC solution with a more relaxed REMA blade precision spec of 15 μ m. In the case of the etched ML border, the simulated CD error stays <1% up to a position error of 40 μ m. The 70nm absorber border would require a tighter REMA blade position precision spec, this spec relaxes for the thicker 84nm absorber, and the etched ML border is the most tolerant to positioning errors.

4.3.3 Stable OoB contribution

In this study the OoB contribution will only be evaluated for the etched ML border for the sake of simplicity. It is assumed that only OoB radiation is reflecting from the substrate of the etched ML border and is the sole cause of the field edge effects for this case. The OoB contribution will be modeled as residual EUV radiation. As shown in Figure 32, it is possible to calibrate a flaremap to model the field edge effects for the etched ML border case. Using the method described in section 3.2.5, the amount of OoB can be controlled for simulation purposes. Over time, IMEC has made OoB radiation measurements on their ASML NXE:3100 that uses a discharge produced plasma (DPP) source. These measurements were made as described in section 3.1.3. Over the course of a year OoB measurements (Figure 44) have been made on the tool to show an OoB contribution ranging from 1.6% to 3.5% [52].

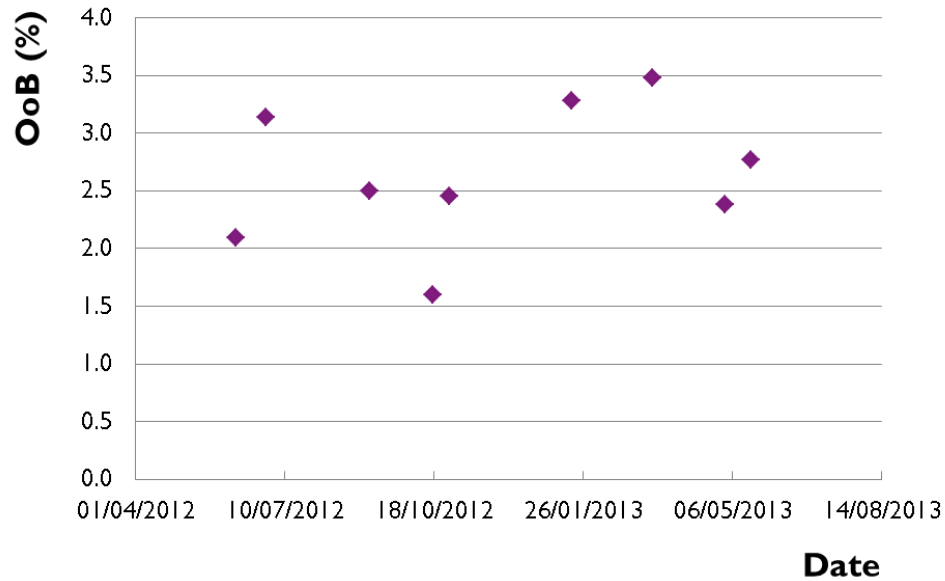


Figure 44. Measurement of OoB component for IMEC's NXE:3100.

Knowing this range, it is possible to make an estimation of how the contact hole CD will change by changing the percentage of OoB. It will be assumed that the measurement data for the etched ML border is at the center of the OoB range to provide the best conditions to apply OPC at. With the OPC completed for this condition for contact holes in the upper left corner of the field, the OoB will then be varied to see how much OoB variability would be tolerable. Figure 45 shows how the CD of the 36nm dense contact holes will be affected by any OoB variability. The red bar shows the range for the expected OoB variability for this tool. From this, one can expect up to 1.7% CD error, which is too high for this application. To keep the CD variation below 1% the total range of OoB contribution must be kept below 1%. Therefore, further improvements to the source are required. It will be of interest to also evaluate the OoB contribution from a LPP source.

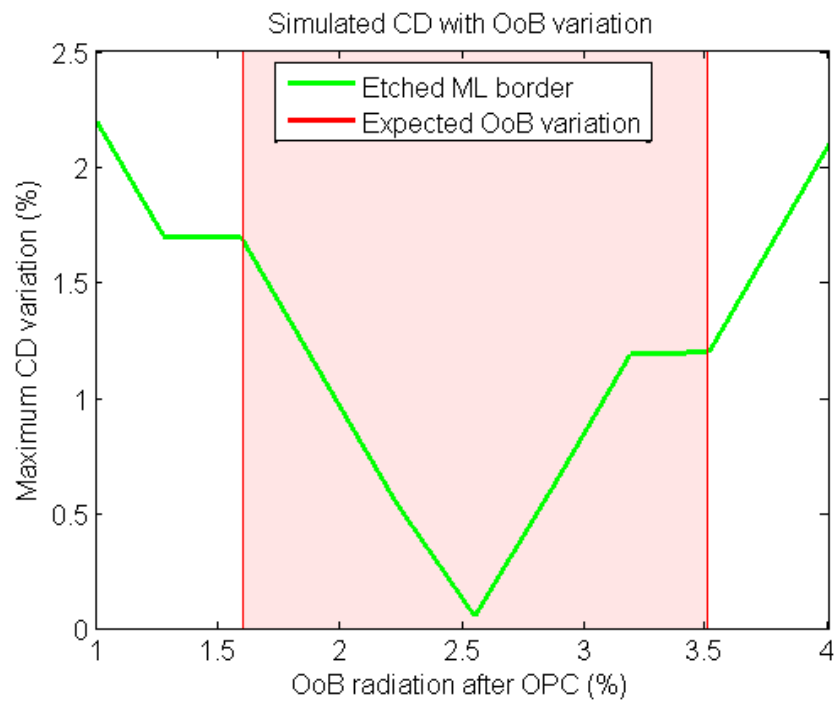


Figure 45. Simulated CD variation for etched ML border when OoB radiation varies after correcting with OPC at the center of the OoB radiation range.

5. Alternative Mitigation Strategy

As learned from this study, mitigating field edge effects can be done by suppressing the EUV and OoB (DUV) reflectivity in the border region. Field edge effects are a direct result of this reflectivity, and act in a similar fashion to flare. For features seeing these effects, their contrast will reduce and CD will change depending on the amount of reflectivity in the border region. Reducing the reflectivity in the border region also suppresses the CD sensitivity to REMA blade positioning errors. OPC can only be used conservatively for corrections of field edge effects. From the results of this work, a new mitigation strategy competitive to the etched ML border should be investigated. One idea would be to apply a thicker absorber to reduce EUV and potentially DUV reflectivity, but only in the border region (Figure 46). This would reduce the field edge effect, while still limiting the amount of shadowing that is seen inside the field. The only drawback of this option is the manufacturability. To manufacture a reticle with two different absorber thicknesses would require an etch-stop layer to produce two different absorber thicknesses.

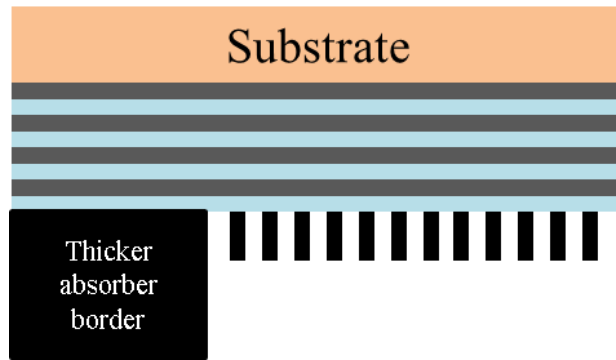


Figure 46. Thicker absorber border potential mitigation strategy.

6. Conclusions

To enable high volume manufacturing for EUV lithography, field edge effects must be mitigated. As the insertion point of EUV lithography continues to be pushed further and further back, some of the key problems preventing its insertion must be uncovered and solved. This thesis introduced the concept of field edge effects and provided some insight into how one could correct for these effects. OPC offers one possible solution, but its feasibility had not been investigated before this work. Three reticles were studied since each one results in different magnitudes of field edge effects. Measurements were made on the NXE:3100 using one of the reticles to prove that the field edge effects could be modeled physically, and therefore it was possible to extrapolate the modeling to other reticles. Correction with OPC was also investigated to see if it could be used in combination with another mitigation strategy that utilizes an etched ML border. For each case, the image quality was analyzed to see if applying OPC corrections is even feasible. In addition, the sensitivity to REMA blade positioning errors was also discussed. Furthermore, for the etched ML border, the effect of OoB variability was studied to show its impact on the printed CD. It was concluded that for each reticle a slightly different mitigation strategy would be required. Therefore, one solution would not be sufficient and the best strategy would be reticle dependent. Not only did this work uncover some possible solutions using existing technology, but an additional mitigation strategy was also discussed as a result of the learnings from this investigation.

Two masks were used to make exposures on the NXE:3100 at IMEC. One was a Hoya reticle with a 70nm absorber and the second was a Hoya reticle with a 70nm absorber with an etched ML border to eliminate EUV reflections in the border region. 36nm dense contact holes were printed at various distances from the field edges and corners. The 70nm Hoya absorber showed a 25% increase in CD from the center of the field to the corner as a result of three overlapping neighboring fields. The etched ML border reticle was expected to show no CD change but actually resulted in a 2.5% CD shift from field center to corner. This was assumed to be the result of OoB radiation reflecting off the mask substrate. Over time, this OoB radiation was measured to monitor how it varied over time, and was measured to vary randomly anywhere from 1.5% to 3.6%.

For the 70nm Hoya reticle, measurements were made and Mentor Graphics' Calibre software was used to fit a model to this data. Knowing the absorber EUV and DUV reflectivity it is possible to extrapolate this model to other reticles, and that was done for a 51nm Hoya absorber and also an 84nm AGC absorber. The model was also calibrated to fit to the etched ML border data. For each case, it was assumed that the models were for data at the center of the expected REMA blade position distribution and also at the center of the OoB variability range. This provided the best possible location to apply OPC at.

Next, the image quality was studied for each reticle after being corrected with OPC, both at the center of the field and then in the corner of the field where three

overlapping fields provided a worst case scenario. For the 51nm Hoya absorber and 70nm Hoya absorber, a loss in contrast prevented the feasibility of correcting for field edge effects with OPC. In the 51nm Hoya absorber case, this shrunk the process window below the requirements. For the 70nm Hoya absorber, a significant degradation in LCDU was the main factor preventing OPC correction in the corner of the field. On the contrary, the 84nm AGC absorber maintained good image quality to enable correction of field edge effects with OPC.

The REMA blade positioning errors were then studied to investigate the impact they would have on an OPC corrected field corner. After OPC correction with a nominal REMA blade position, it was concluded that the 70nm Hoya absorber would require tighter specifications of $<5\mu\text{m}$ precision on the REMA blades to provide an acceptable solution. Out of all of the absorber borders, the 84nm AGC absorber performed the best for the measured REMA blade precision values, requiring a REMA blade precision spec of about $15\ \mu\text{m}$. The etched ML border reticle actually had the least CD variation from REMA blade positioning errors.

In terms of OoB stability, only the etched ML border reticle was investigated. The OoB contribution was controlled by adjusting the ratio of the residual EUV to the desired OoB contribution. It was assumed that the OPC correction was for an OoB contribution that was at the center of the measured range. The percentage of OoB was then varied across this range to see the impact that it would have on the CD. At the edge of the range, a 1.7% CD error was found, which would be too high for this application. To keep the

CD variability below 1%, the total OoB variability range would need to be limited to <1%.

To summarize the results of this work, each reticle would require a different mitigation strategy. To mitigate the field edge effects, the 51nm Hoya and 70nm Hoya absorbers would not be correctable solely with OPC but would require an additional mitigation strategy such as etching the ML in the border region. If the etched ML border solution were to be implemented it would require a tighter specification on the OoB variability than what was measured from the DPP source at IMEC. The 84nm AGC absorber would require only correction with OPC and results in good image quality and would require a looser REMA blade tolerance spec.

Mitigating field edge effects depends completely on the reflectivity of EUV and OoB radiation in the border region of the reticle. The 84nm AGC absorber results in the least amount of EUV reflectivity and therefore the field edge effects can possibly be corrected for with OPC alone. The 51nm and 70nm Hoya absorbers have a bit higher EUV reflectivity and would therefore require an additional mitigation strategy such as the etched ML border, which still has results in a measurable field edge effect from OoB radiation.

This thesis shows that through simulation, OPC can be used to correct for field edge effects, but the fashion that it is applied is reticle dependent. Going forward, it is desirable to only have to rely on OPC conservatively since it may add minimal but still unwanted errors from the REMA blade positioning and also creates a problem when

printing die at the edges of the wafer that do not have overlapping neighboring fields. These die at the edges of the wafer would require different OPC. In addition, it is not desirable to use thicker absorbers since they result in additional shadowing errors. This leaves room for lithographers to be creative. At some point, the field edge effect should be mitigated entirely without OPC, one idea to do this would be to implement a reticle with a thick absorber only in the border region.

7. References

-
- [1] “John Bardeen, William B. Shockley, and Walter H. Brattain and the Invention of the Transistor.” [Online]. Available: <http://www.aps.org/programs/outreach/history/historicsites/transistor.cfm>. [Accessed: 12-Sep-2013].
- [2] “The Chip that Jack Built | Jack Kilby | Innovation | Company | About TI.” [Online]. Available: <http://www.ti.com/corp/docs/kilbyctr/jackbuilt.shtml>. [Accessed: 12-Sep-2013].
- [3] L. J. W and N. J. R, “Semiconductor construction,” US2890395 A09-Jun-1959.
- [4] A. Jules, “Fabrication of semiconductor devices,” US3122817 A03-Mar-1964.
- [5] Y. Borodovsky, “Marching to the beat of Moore’s Law,” 2006, vol. 6153, pp. 615301–615301–19.
- [6] J. H. Bruning, “Optical lithography--thirty years and three orders of magnitude: the evolution of optical lithography tools,” 1997, vol. 3051, pp. 14–27.
- [7] J. H. Bruning, “Optical lithography: 40 years and holding,” 2007, vol. 6520, pp. 652004–652004–13.
- [8] “The Story of the Intel® 4004,” *Intel*. [Online]. Available: <http://www.intel.com/content/www/us/en/history/museum-story-of-intel-4004.html>. [Accessed: 12-Sep-2013].
- [9] “Intel Delivers New Architecture for Discovery with Intel® Xeon Phi™ Coprocessors,” *Intel Newsroom*. [Online]. Available: http://newsroom.intel.com/community/intel_newsroom/blog/2012/11/12/intel-delivers-new-architecture-for-discovery-with-intel-xeon-phi-coprocessors. [Accessed: 12-Sep-2013].
- [10] R. L. Easton Jr., *Fourier Methods in Imaging*, 2nd ed. Wiley, 2010.
- [11] J. W. Goodman, *Introduction to Fourier Optics*, 3rd ed. Roberts & Company Publishers, 2004.
- [12] K. Suzuki and B. Smith, Eds., *Microlithography: Science and Technology, Second Edition*, 2nd ed. CRC Press, 2007.
- [13] A. J. den Dekker and A. van den Bos, “Resolution: a survey,” *J. Opt. Soc. Am.*, vol. 14, no. 3, pp. 547–557, Mar. 1997.
- [14] Lord Rayleigh, “Investigations in optics, with special reference to the spectroscope,” *Mon. Not. R. Astron. Soc.*, vol. 40, p. 254, Feb. 1880.
- [15] B. W. Smith, “The saga of lambda: spectral influences throughout lithography generations,” 2012, vol. 8325, p. 83250Z–83250Z–9.
- [16] Rayleigh, “XV. On the theory of optical images, with special reference to the microscope,” *Philos. Mag. Ser. 5*, vol. 42, no. 255, pp. 167–195, 1896.

- [17] F. M. Schellenberg, "Resolution enhancement technology: the past, the present, and extensions for the future," presented at the Society of Photo-Optical Instrumentation Engineers (SPIE) Conference Series, 2004, vol. 5377, pp. 1–20.
- [18] S. Matsuo, K. Komatsu, Y. Takeuchi, E. Tamechika, Y. Mimura, and K. Harada, "High resolution optical lithography system using oblique incidence illumination," in *Electron Devices Meeting, 1991. IEDM '91. Technical Digest., International*, 1991, pp. 970–972.
- [19] B. W. Smith, L. V. Zavyalova, and A. Estroff, "Benefiting from polarization effects on high-NA imaging," 2004, vol. 5377, pp. 68–79.
- [20] A. E. Rosenbluth, S. J. Bukofsky, M. S. Hibbs, K. Lai, A. F. Molless, R. N. Singh, and A. K. K. Wong, "Optimum mask and source patterns to print a given shape," 2001, pp. 486–502.
- [21] B. E. Saleh, "Reduction Of Errors Of Microphotographic Reproductions By Optimal Corrections Of Original Masks," *Opt. Eng.*, vol. 20, no. 5, p. 205781, Oct. 1981.
- [22] K. Maruyama, "Recent progress in chemically amplified extreme UV resist technology," *SPIE Newsroom*, Jan. 2011.
- [23] M. Kempell Sears and B. W. Smith, "Pupil wavefront manipulation to compensate for mask topography effects in optical nanolithography," 2013, vol. 8683, p. 86830G–86830G–12.
- [24] K. Murakami, T. Oshino, H. Kondo, M. Shiraishi, H. Chiba, H. Komatsuda, K. Nomura, and J. Nishikawa, "Development progress of optics for extreme ultraviolet lithography at Nikon," *J. MicroNanolithography MEMS MOEMS*, vol. 8, no. 4, pp. 041507–041507–6, 2009.
- [25] H. E. BENNETT and J. O. PORTEUS, "Relation Between Surface Roughness and Specular Reflectance at Normal Incidence," *J. Opt. Soc. Am.*, vol. 51, no. 2, pp. 123–129, Feb. 1961.
- [26] J. F. Chen, T. L. Laidig, K. E. Wampler, and R. F. Caldwell, "Practical method for full-chip optical proximity correction," 1997, vol. 3051, pp. 790–803.
- [27] A. Starikov, "Use Of A Single Size Square Serif For Variable Print Bias Compensation In Microlithography: Method, Design, And Practice," 1989, vol. 1088, pp. 34–47.
- [28] P. J. Silverman, "Extreme ultraviolet lithography: overview and development status," *J. MicroNanolithography MEMS MOEMS*, vol. 4, no. 1, pp. 011006–011006–5, 2005.
- [29] B. L. Henke, E. M. Gullikson, and J. C. Davis, "X-Ray Interactions: Photoabsorption, Scattering, Transmission, and Reflection at $E = 50\text{--}30,000$ eV, $Z = 1\text{--}92$," *At. Data Nucl. Data Tables*, vol. 54, no. 2, pp. 181–342, Jul. 1993.
- [30] J. Stoeldraijer, D. Ockwell, and C. Wagner, "EUVL into production – Update on ASML's NXE platform," *Int. Symp. Extreme Ultrav. Lithogr.*, Oct. 2009.
- [31] A. Vaglio Pret, K. Garidis, R. Gronheid, and J. Biafore, "Stochastic limitations for EUV resist kinetics towards the 16nm node," *Int. Symp. Extreme Ultrav. Lithogr.*, Oct. 2011.

- [32] J. T. Neumann, P. Gräupner, W. Kaiser, R. Garreis, and B. Geh, "Mask effects for high-NA EUV: impact of NA, chief-ray-angle, and reduction ratio," 2013, vol. 8679, pp. 867915–867915–13.
- [33] P. C. W. Ng, K.-Y. Tsai, Y.-M. Lee, T.-H. Pei, F.-M. Wang, J.-H. Li, and A. C. Chen, "A fully model-based methodology for simultaneously correcting EUV mask shadowing and optical proximity effects with improved pattern transfer fidelity and process windows," 2009, vol. 7520, p. 75200S–75200S–12.
- [34] M. Sugawara, T. Hashimoto, and I. Nishiyama, "Effect of absorber material and mask pattern correction on pattern fidelity in EUV lithography," 2004, vol. 5374, pp. 289–299.
- [35] S. Raghunathan, G. McIntyre, G. Fenger, and O. Wood, "Mask 3D effects and compensation for high NA EUV lithography," 2013, vol. 8679, pp. 867918–867918–13.
- [36] T. Suzuki, T. Hori, T. Yanagida, T. Yabu, H. Nagano, Y. Wada, S. Georg, J. Fujimoto, and H. Mizoguchi, "Investigation on high conversion efficiency and Tin debris mitigation for laser produced plasma EUV light source," *Int. Symp. Extreme Ultrav. Lithogr.*, Oct. 2011.
- [37] A. J. R. van den Boogaard, E. Louis, F. A. van Goor, and F. Bijkerk, "Optical element for full spectral purity from IR-generated EUV light sources," *Int. Symp. Extreme Ultrav. Lithogr.*, Oct. 2011.
- [38] M. D. Smith, "Stochastic Resist Simulation for EUV," presented at the 2010 International Workshop on EUV, Maui, Hawaii, Jun-2010.
- [39] C. A. Mack, J. W. Thackeray, J. J. Biafore, and M. D. Smith, "Stochastic exposure kinetics of extreme ultraviolet photoresists: simulation study," *J. MicroNanolithography MEMS MOEMS*, vol. 10, no. 3, pp. 033019–033019–11, 2011.
- [40] W. Schottky, "Über spontane Stromschwankungen in verschiedenen Elektrizitätsleitern," *Ann. Phys.*, vol. 362, no. 23, pp. 541–567, 1918.
- [41] G. E. Bailey, A. Tritchkov, J.-W. Park, L. Hong, V. Wiaux, E. Hendrickx, S. Verhaegen, P. Xie, and J. Versluijs, "Double pattern EDA solutions for 32nm HP and beyond," 2007, vol. 6521, p. 65211K–65211K–12.
- [42] V. Wiaux, S. Verhaegen, S. Cheng, F. Iwamoto, P. Jaenen, M. Maenhoudt, T. Matsuda, S. Postnikov, and G. Vandenberghe, "Split and design guidelines for double patterning," 2008, vol. 6924, pp. 692409–692409–11.
- [43] P. Zimmerman, "Double patterning lithography: double the trouble or double the fun?," *SPIE Newsroom*, 2009.
- [44] K. Takai, K. Murano, E. Yamanaka, S. Yamaguchi, M. Naka, T. Kamo, and N. Hayashi, "Improvement of EUVL mask structure with black border of etched multilayer," 2013, vol. 8701, p. 87010Y–87010Y–8.
- [45] N. Fukugami, K. Matsui, G. Watanabe, T. Isogawa, S. Kondo, Y. Kodera, Y. Sakata, S. Akima, J. Kotani, H. Morimoto, and T. Tanaka, "Black border with etched multilayer on EUV mask," presented at the Society of Photo-Optical Instrumentation Engineers (SPIE) Conference Series, 2012, vol. 8441.

- [46] N. Davydova, E. van Setten, R. de Kruif, D. Oorschot, M. Dusa, C. Wagner, J. Jiang, W. Liu, H. Kang, H. Liu, P. Spies, N. Wiese, and M. Waiblinger, "Imaging performance improvements by EUV mask stack optimization," 2011, vol. 7985, p. 79850X–79850X–13.
- [47] C. H. Clifford, Y. Zou, A. Latypov, O. Kritsun, T. Wallow, H. J. Levinson, F. Jiang, D. Civay, K. Standiford, R. Schlieff, L. Sun, O. R. Wood, S. Raghunathan, P. Mangat, H. P. Koh, C. Higgins, J. Schefske, and M. Singh, "EUV OPC for the 20-nm node and beyond," p. 83221M–83221M, Mar. 2012.
- [48] G. F. Lorusso, N. Davydova, M. Eurlings, C. Kaya, Y. Peng, K. Feenstra, T. H. Fedynyshyn, O. Natt, P. Huber, C. Zaczek, S. Young, P. Graeupner, and E. Hendrickx, "Deep ultraviolet out-of-band contribution in extreme ultraviolet lithography: predictions and experiments," 2011, p. 79692O–79692O–8.
- [49] W. Gao, A. Niroomand, G. F. Lorusso, R. Boone, K. Lucas, and W. Demmerle, "Simulation study of CD variation caused by field edge effects and out-of-band radiation in EUVL," 2013, vol. 8880, p. 88800H–88800H–11.
- [50] J. Mailfert, G. F. Lorusso, J. Van de Kerkhove, P. Debisschop, V. Philipsen, C. Zuniga, K. Adam, M. Lam, J. Word, and E. Hendrickx, "OPC calibration for pre-production EUVL," *Int. Symp. Extreme Ultrav. Lithogr.*, Oct. 2012.
- [51] N. Davydova, R. de Kruif, H. Morimoto, Y. Sakata, J. Kotani, N. Fukugami, S. Kondo, T. Imoto, B. Connolly, D. van Gestel, D. Oorschot, D. Rio, J. Zimmerman, and N. Harned, "Impact of an etched EUV mask black border on imaging: part II," 2013, vol. 8880, pp. 888027–888027–12.
- [52] E. Hendrickx, "ASML NXE:3100 Pre-Productino EUV Scanner Performance at imec," presented at the EUVL Symposium, Toyama, Japan, Oct-2013.